

Bachelor Assignment
High Capacitance Thin Films

Christoph Chmiel

July 8, 2011

Summary

A capacitance test circuit using strontium titanate as dielectric material was produced by means of modern thin film deposition techniques. The capacitance per area was measured by using two different measurement techniques. The quasistatic value was found to be $C/A = 4.70 \pm 0.03 \mu\text{F}/\text{cm}^2$ and the value at a frequency of 1kHz was found to be $C/A = 3.85 \pm 0.08 \mu\text{F}/\text{cm}^2$. A characterization of these films with the use of atomic force microscopy and x-ray diffraction was done.

To increase these values even further, strontium doped barium titanate targets for the use in laser ablation systems were produced by using the solid state synthesis method at a temperature of 1200°C. Since this material is normally sintered at higher temperatures a polyvinyl alcohol had to be used to produce stable targets. The purity of these targets was checked with a x-ray diffraction scan after each process step.

Two types of stoichiometry were produced: $\text{Ba}_{0.5}\text{Sr}_{0.5}\text{TiO}_3$ and $\text{Ba}_{0.67}\text{Sr}_{0.33}\text{TiO}_3$. A crack was found in the latter one and so only the former could be tested in a laser ablation device. With a deposition temperature of 700°C the growth speed was determined to be 0.037 nm/pulse in an 0.13 mbar oxygen atmosphere by using laser energy density of 1.5 J/cm² from a KrF excimer laser operating at a wavelength of 248nm.

Contents

1	Introduction	1
1.1	The need for high capacitance thin films	1
2	Theoretical Background	3
2.1	Capacitors	3
2.1.1	Capacitance	3
2.1.2	Behavior of a capacitor	4
2.1.3	Capacitance measurement	5
2.2	Materials	7
2.2.1	Crystal structures and properties of used materials	7
2.3	Material analysis techniques	10
2.3.1	Scanning electron microscope	10
2.3.2	Atomic force microscopy	10
2.3.3	X-ray spectroscopy	11
2.4	Thin film deposition techniques	12
2.4.1	Pulsed laser deposition	12
2.4.2	RF sputtering	13
3	Experimental Work	15
3.1	Production of a capacitance test circuit	15
3.1.1	Sample structure	15
3.1.2	Thin film circuit preparation	16
3.2	Solid state synthesis of barium strontium titanate targets for use in laser ablation devices	18
3.2.1	Reaction and processing	18
3.3	Target testing and film growth	21
3.3.1	Determination of energy flux	21
3.3.2	Film deposition of BSTOx5	23
4	Results and discussion	25
4.1	Capacitance test circuit	25
4.1.1	Production	25
4.1.2	Capacitance measurements	26
4.2	Barium strontium titanate targets for the use in laser ablation growth techniques	28
4.2.1	Target Preparation	28

4.2.2 Grown Films	29
5 Conclusions and Final remarks	31
5.1 Conclusions	31
5.2 Future outlook	31
A Device settings	33
A.1 Production of the capacitance test circuit	33
A.2 Film growth of barium strontium titanate	39
B X-ray diffraction scans	41
Bibliography	45

Chapter 1

Introduction

1.1 The need for high capacitance thin films

In our century, due to the extraordinary rapid growth of technology, people are getting more and more used to gadgets like mobile phones, global positioning devices and of course the nowadays almost ordinary computer. In a modern western household such devices have established as standard inventory. Because of this high demand on data processing devices the need of producing these devices cost-efficient speaks for itself. In this context Moore's Law¹ is often quoted and the limitations of manufacturing these devices are pointed out.

As the structures continue to shrink new problems come to pass that were not present before. Among others, one problem is the thickness of the gateoxide used in the more and more shrinking transistor structures. With decreasing thickness, the capacity decreases and the possibility of quantum mechanical tunneling of charge carriers through the gateoxide increases. Both effects are clearly unwanted. Besides the use in transistors, dielectric thin films are also used for basic energy storage on integrated circuits in the form of capacitors.

It is the aim of this project to look for the possibilities of manufacturing and measurement of high capacitance structures within the research group Interfaces and Correlated Electron systems of the University of Twente, Netherlands. In the course of the project several techniques involving thin film growth, structuring and analysis were used to achieve this goal. A high dielectric material was synthesized for the use in such thin film capacitance structures.

¹Moore's law predicts the annual growth of the number of transistors placed on an integrated circuit [7]

Chapter 2

Theoretical Background

Throughout this thesis, there will be made use of some principles that require a certain knowledge. This chapter therefore intends to give the necessary background information to the reader. References are given, for those who want to get deeper insight in the processes described here.

2.1 Capacitors

2.1.1 Capacitance

When two metal conductors face each other in vacuum, with charge $+Q$ on one and $-Q$ on the other, an electric field \mathbf{E} is created that can be described by the potential difference ΔV between the conductors. If now the amount of charge is changed the potential is expected to change, too. The constant of proportionality between the charge and the potential is called the Capacitance C and is defined by

$$C \equiv Q/V. \quad (2.1)$$

The capacitance in vacuum is a purely geometrical quantity that depends on shape, size and separation distance of the conductors. From Gauss's law the vacuum capacitance of a configuration where the conductors are two plates of equal size A lying parallel to each other, with separation d we find that the capacitance is

$$C = \frac{A\epsilon_0}{d}. \quad (2.2)$$

Where ϵ_0 is the *constant of permittivity in vacuum*. This configuration is called a *Parallel Plate Capacitor* and is shown in figure 2.1. It is the most common way to store electrical energy in circuit designs that are used in everyday electronics.

When a dielectric material is placed between the two conductors (or electrodes) the positive and negative charged ions inside the dielectric will align themselves due to the force of electric field. This creates many little dipoles which point all in the same direction. The material is now described as being electrically polarized. When dealing with linear materials this Polarization is proportional to the electric field and the ϵ_0 in eq. 2.2 has to be changed to

$$\epsilon = \epsilon_r \epsilon_0 \quad (2.3)$$

2. Theoretical Background

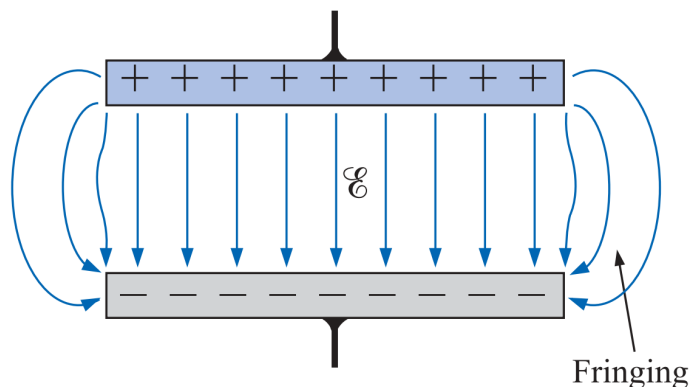


Figure 2.1: A parallel plate capacitor, the blue arrows illustrate the electric field between the two plates. The fringing fields just at the very edge of the plates are neglected in the analysis.

where ϵ_r is the ratio of the constant of permittivity in matter (more precise the material in question) to the one in vacuum. It follows that, compared to the vacuum capacitance, the capacitance is increased by a factor of the dielectric constant $C = \epsilon_r C_O$. Note that ϵ_r is a material dependent property which is therefore also dependent on the direction of the crystal growth and temperature. There might also be a dependence on the frequency of the applied electric field. It is this constant that is of main concern in this Bachelor thesis.

2.1.2 Behavior of a capacitor

The simplest configuration of a capacitor used in an electric circuit is to place it in series with a resistor. This is shown in figure 2.2.

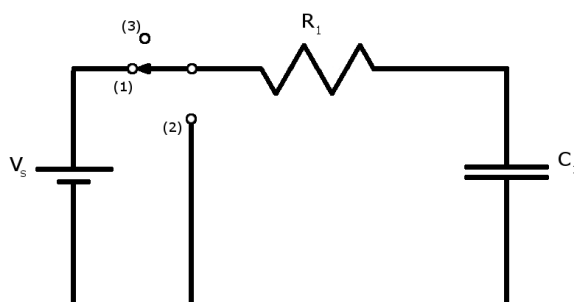


Figure 2.2: A series circuit of a resistance R_1 and an ideal capacitance C

When a voltage V_s is applied and the switch is in position (1) the capacitor will be charged up. As can be obtained from circuit analysis¹ the voltage over the capacitor will behave according to

$$V_c = V_s(1 - e^{t/\tau}) \quad (2.4)$$

¹More information on circuit analysis can be found in [1]

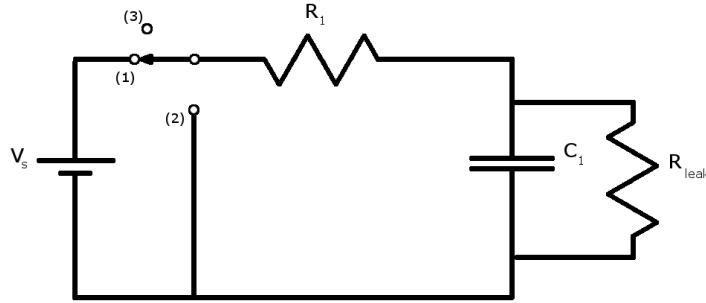


Figure 2.3: The model circuit of a real capacitor in an RC configuration

Where $\tau = R_1 C$ is a time constant of the circuit. From this equation it is clear that the voltage across a capacitor cannot change instantaneously. When the switch is put into position (2) the capacitor will discharge. There is no electromotive force present to push charges on to the electrodes and so they will distribute themselves to reach an equilibrium state. Therefore they flow through the resistance, which in turn dissipates the energy in the form of heat to the surroundings. The voltage characteristic in this case behaves according to

$$V_c = V_s e^{-t/\tau}. \quad (2.5)$$

When the switch is in position (3) there is no chance for the charges to reach the other electrode and thereby form an equilibrium state. The charges will stay on the electrodes and it is said, that the capacitor stores the electric energy.

Actually this only holds for an ideal capacitor. The correct behavior can be described through modeling the capacitor together with a parallel resistance that represents the leakage load as shown in figure 2.3. Because of the parallel resistance the characteristics of the voltage over the capacitor change slightly. The correct expression for the voltage, when a charging voltage V_s is applied (switch in position (1)), is now given by

$$V_c = V_s \frac{R_{leak}}{R_1 + R_{leak}} (1 - e^{-\tau_1 t}) \quad \text{with} \quad \tau_1 = \frac{1}{C} \left(\frac{R_1 + R_{leak}}{R_1 R_{leak}} \right) \quad (2.6)$$

By switching to position (2), the capacitor now discharges according to equation 2.5 but now with $\tau = 1/C(1/R_1 + 1/R_{leak})$.

2.1.3 Capacitance measurement

For measuring the capacitance of the test circuit two devices were used that work with different measurement techniques. One does a quasistatic measurement and the other does a frequency measurement. The working principles that were described in the manuals ([10] and [11]) of the devices are summarized here.

Quasistatic CV measurements with the Keithley Model 595 Quasistatic CV meter The Keithley Quasistatic CV meter uses a feedback charge measurement to calculate the capacity of a device. A schematic diagram of the working of this method is depicted in figure 2.4. This method works as follows. First by closing switch S the

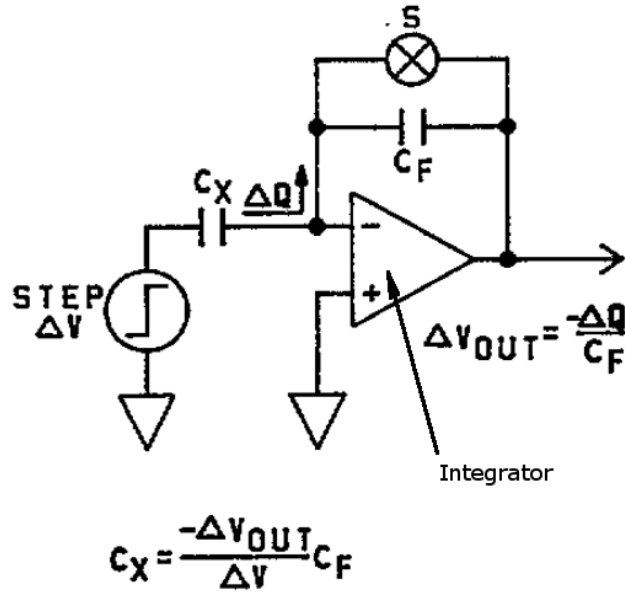


Figure 2.4: A schematic diagram of the quasistatic CV measurement technique. Picture taken from the Keithley Model 595 instructions manual [10].

feedback capacitor is short circuited to discharge it completely. When the switch is opened again the voltage (V_{out}) over the feedback capacitor is given by

$$\Delta V_{out} = \frac{\Delta Q}{C_f}. \quad (2.7)$$

Where ΔQ is calculated by integrating the current. Now a voltage pulse of fixed height is applied over the capacitor in question whose Voltage is given by

$$\Delta V = -\frac{\Delta Q}{C_x}. \quad (2.8)$$

Solving these two equations for C_x the capacity of the device to be measured follows as

$$C_x = -\frac{C_f \Delta V_{out}}{\Delta V}. \quad (2.9)$$

Measurements with the Philips PM 6303 RCL Meter The Philips RCL meter uses a technique called current and voltage method and can measure the resistance, capacitance or inductance of a device. After the measurement is done, an internal CPU calculates the strongest signal and sends it to the readout display.

First, an alternating current of 1kHz is applied to the component that has to be measured. It then measures the current and voltage, first a phase angle of 0° and then again with a phase angle of 90° .² From these values it calculates the resistance (R),

²These values are equivalent to the real and imaginary parts of the alternating current and voltage measured.

reactance (X) and the quality factor (Q) of the component according to the following formulas

$$R = \frac{V_p I_p + V_q I_q}{I_p^2 + I_q^2}, \quad (2.10)$$

$$X = \frac{V_p I_q + V_q I_p}{I_p^2 + I_q^2}, \quad (2.11)$$

$$Q = \frac{|X|}{R}, \quad (2.12)$$

where the subscript p denotes the 0° phase angle measurement and the subscript q denotes the 90° phase angle measurement. From this measurements the CPU determines the strongest component and gives in the case of a strong signal for capacitance the value according to the following formula

$$C = \frac{1}{\omega(1 + 1/Q^2)|X|}. \quad (2.13)$$

Wherein ω is the angular frequency that is related to the frequency of the alternating current by $\omega = 2\pi f$.

2.2 Materials

2.2.1 Crystal structures and properties of used materials

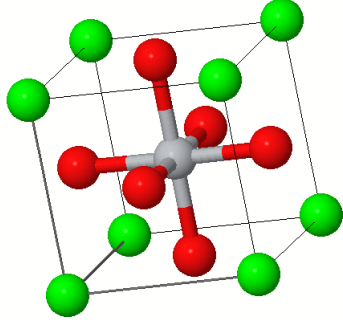
For building a thin film capacitance structure there are certain aspects that have to be taken into account. For example, the lattice constant of the materials, which are grown on top of each other, should match so that there is no deformation of the unit cells. This way there is no stress induced in the films and the electrical properties won't be disturbed. The choice of the materials used in the experiments and their properties are described in what follows.

It is well known in literature that ceramic materials are well suited as a dielectric in a capacitor configuration. Because of their para electric behavior they have a high tendency to get polarized. When the material is subjected to an electric field, the ions in the crystal lattice will shift away from their original positions. After the field is removed they will return to their original positions³. A perfect example of such a material is strontium titanate, which was used for fabricating a thin film structure in the course of this bachelor assignment.

Strontium titanate Strontium titanate SrTiO_3 (in the following named STO) is at room temperature a para electric ceramic with a cubic crystal structure of the perovskite type as shown in figure 2.5. It has a lattice constant of 3.9034 \AA . It is known for it's high dielectric constant in the order of 330 [2]. These values are also summarized in figure 2.5. STO was chosen for the production of a high capacitance test sample because the growth conditions were well known in the group. It also has a low misfit with yttrium barium

³This holds only for linear dielectric materials in a static environment. Non linear behavior will be explained briefly later on.

2. Theoretical Background



Strontium titanate	
Unit cell structure:	perovskite (cubic)
Lattice constant:	3.9034 Å
Dielectric constant:	~ 330 @ RT
Misfit grown on (001) YBCO	f=-0.0053 (a-axis) f=-0.0211 (b-axis)
Barium_x strontium_{1-x} titanate	
• x=0.5	
Unit cell structure:	perovskite (cubic)
Lattice constant:	3.9613 Å
Dielectric constant:	~480@ RT [14]
• x=0.67	
Unit cell structure:	perovskite (cubic)
Lattice constant:	3.9809 Å
Dielectric constant:	~1503 @ RT [13]

Figure 2.5: Unit cell of a cubic perovskite lattice and of strontium titanate and barium strontium titanate. The green balls represent the Ba^{2+} or Sr^{2+} cations, the gray ball Ti^{4+} cations and the red balls are the O^{2-} anions.

copper oxide (see below) that was used as electrode. The misfits in the [001] direction of yttrium barium copper oxide are $f=-0.0053$ (a-axis) and $f=-0.0211$ (b-axis).

Strontium doped Barium titanate Strontium doped barium titanate $\text{Ba}_x\text{Sr}_{1-x}\text{TiO}_3$ (in the following named BSTO) is in contrast to STO either a paraelectric⁴ or a ferroelectric⁵ crystal, depending on the doping. The crystal structure is the same perovskite cubic lattice structure as of STO with a lattice constant of 4.0191 Å. It was reported that the transition temperature between the ferroelectric and para electric state, the *ferroelectric Curie temperature*, varies almost linear with the amount of strontium doping from $T_C = 40\text{K}(x = 0)$ to $T_C = 415\text{K}(x = 1)$ [3]. As shown in figure 2.6 the dielectric constant peaks at this very temperature. So for a device operating at room temperature the ratio of Ba/Sr has to be adjusted in order to gain maximum efficiency. Because the effects of ferroelectricity are unwanted in a simple capacitance setup, this has to be done in such a way that T_C lies just below room temperature as indicated in figure 2.6. From this it can be calculated that at room temperature the ratio of Ba:Sr has to be 2:1.

Yttrium barium copper oxide Yttrium barium copper oxide $\text{YBa}_2\text{Co}_3\text{O}_7$ (in the following named YBCO) is a chemical compound that conducts electricity. YBCO gets superconducting below the critical temperature of $T_c = 93\text{K}$ and is therefore classified as a high temperature superconductor. The lattice of YBCO is perovskite based as shown in

⁴A paraelectric material is one which restores the positions of the shifted ions completely after the electric field is removed.

⁵Ferroelectricity occurs because the cations in the lattice are displaced due to lattice vibrations which is called spontaneous polarization. This cation displacement creates an intrinsic polarization which can be permanent. For more information refer to [4].

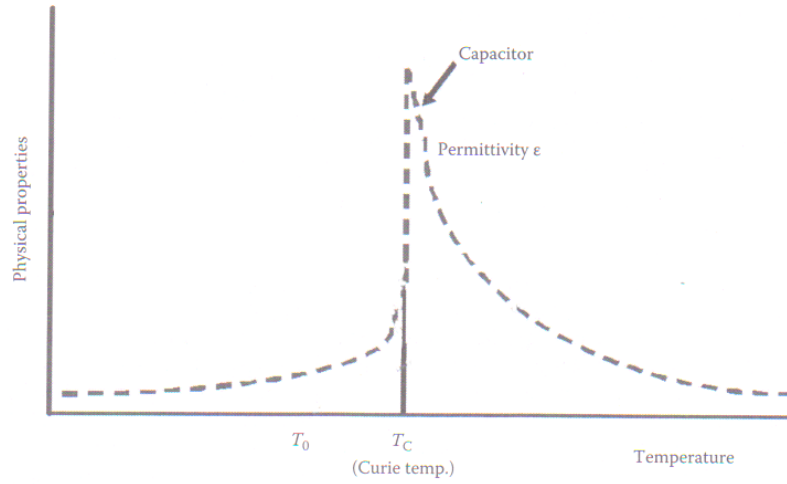


Figure 2.6: The dependency of the dielectric constant on the ferroelectric Curie temperature. Picture taken from Kenji Uchino, Ferroelectric Devices [4].

figure 2.7. The lattice constants are $a=3.8828$, $b=3.8211$ and $c=11.6741$ Å. This material was chosen for the bottom electrode because the growth conditions were well known in the group and, as mentioned earlier, it has a low misfit with STO.

Yttrium barium copper oxide	
Unit cell structure:	perovskite based
Lattice constants:	$a=3.8828$ Å
	$b=3.8211$ Å
	$c=11.6741$ Å
critical Temperature:	$T_c = 93K$

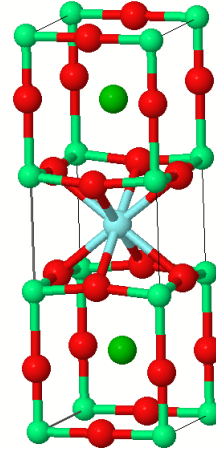
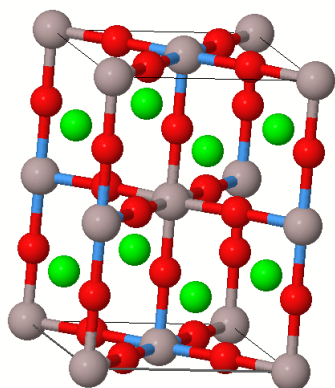


Figure 2.7: The unit cell of the high temperature superconductor yttrium barium copper oxide. Red balls represent oxygen atoms, light greens copper atoms, dark greens barium atoms and aqua coloured yttrium atoms.

Lanthanum aluminum strontium tantalum oxide Lanthanum aluminum strontium tantalum oxide $(\text{LaAlO}_3)_{0.3}(\text{Sr}_2\text{AlTaO}_6)_{0.7}$ (in the following named LSAT) is a dielectric with a cubic perovskite lattice structure. The lattice constant of LSAT is 3.868 Å. In figure 2.8 an alternative unit cell of LSAT is shown where the inner part can be identified as a typical perovskite unit cell as in figure 2.5. LSAT was used as a substrate because it is insulating and has a low misfit with YBCO grown in the [001] direction of about $f=-0.0038$ (a-axis) and $f=0.0123$ (b-axis). Unfortunately, as it turned out, the

2. Theoretical Background

LSAT single crystal substrate was oriented in the [110] direction and thus is the misfit $f=0.4088$ (a-axis) and $f=0.4316$ (b-axis).



Lanthanum aluminum strontium tantalum oxide	
Unit cell structure:	perovskite (cubic)
Lattice constant:	3.868 Å
Dielectric constant:	~ 330 @ RT
Misfit with YBCO grown on (110)	$f=-0.4088$ (a-axis) $f=-0.4316$ (b-axis)

Figure 2.8: An alternative unit cell of lanthanum aluminum strontium tantalum oxide. The red balls represent oxygen atoms, the gray ones aluminum or tantalate and the green ones strontium or lanthanum. In the middle you can identify the basic perovskite structure as in figure 2.5

2.3 Material analysis techniques

2.3.1 Scanning electron microscope

As the name suggests the scanning electron microscope (in the following named SEM) uses an electron ray that scans over the surface of the specimen that is being observed. The electron beam is produced by an electron gun and focused by two electromagnetic lenses. As depicted in figure 2.9a, when the electrons impinge on the specimen they scatter inelastically on the electrons and nucleons of the specimen thereby filling a drop-like shaped region. From this region originate several energetic particles as shown in 2.9b. Most SEMs detect the low energetic secondary electrons that are formed when an incident electron ionizes an atom of the specimen. This occurs for the most part at the surface where the primary electrons still have enough energy. The high contrast of SEM pictures can be explained with a look at figure 2.9c. When the electron beam impinges on a sloping surface, the area of impact perpendicular to that surface is greater. This means that there will be more secondary electrons produced and sloping surfaces thus seem brighter in the pictures.

2.3.2 Atomic force microscopy

The atomic force microscope produces images by moving a probe over the surface of the specimen in question. The probe consists of a cantilever with a good defined resonance frequency and a very sharp tip at the end as depicted in figure 2.10. When the tip is close to the surface it gets attracted (through van der Waals forces) or repelled (due to the overlap of the electron clouds). Because these forces are very weak, the cantilever is set under vibrations. Every change in vibrational amplitude or resonance frequency is

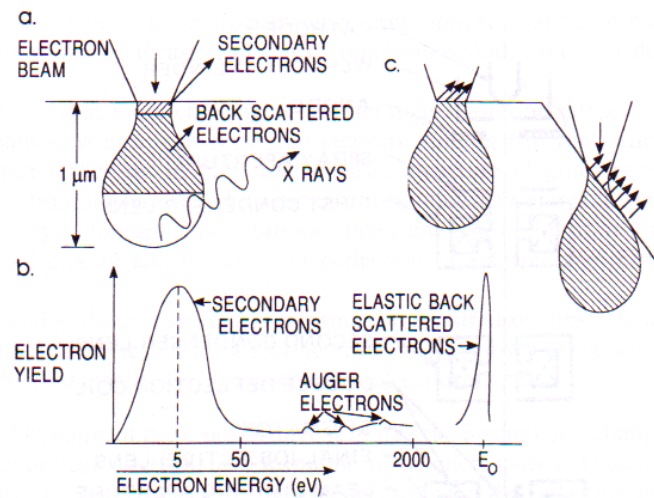


Figure 2.9: Illustration of the drop shaped scattering region inside a specimen due to the impact of an electron beam and the energy spectrum of particles originating from it. Picture taken from Milton Ohring, Materials Science of Thin Films [9].

than monitored via a laser beam. This data can then be converted into a topographic map of the scanned area. The AFM can operate in two modes: non-contact mode and contact mode. In the former the tip chases the vibrations due to attractive forces. To prevent it from crashing into the surface a rather stiff cantilever is used. In the latter the tip actually makes contact with the surface and the reaction on the repulsive forces is recorded.

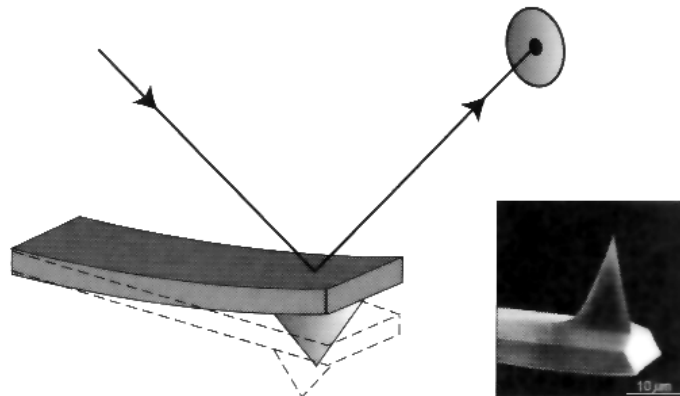


Figure 2.10: The probe of an AFM imaging device. Picture taken from Charles Kittel, Introduction to Solid State Physics [12].

2.3.3 X-ray spectroscopy

This analysis technique uses a beam of photons with a wavelength in the x-ray range to analyze crystal structures. When the photons penetrate into the the material they collide with electrons and get reflected. A detector than looks for those photons which have not

2. Theoretical Background

lost any energy during the collision. Because the electron density is high at the lattice planes of a crystal the scattering amplitude of the x-rays will also be high there. This is schematically depicted in figure 2.11. For the photons that lose no energy the incident angle equals the reflected angle. Since this reflection takes place at all lattice planes, this will lead to constructive interference of the photons if the difference of the path length equals an integer (n) wavelength. From this the well known Bragg law can be derived

$$2d \sin \theta = n\lambda. \quad (2.14)$$

Where λ is the wavelength of the x-rays used.

X-ray spectroscopy can therefore determine the spacing between lattice planes and give information about the directions the crystal is grown. This analysis can also be done on powders where all directions will be recorded. It can therefore be used to check for impurities coming from unwanted crystals. A measurement at glancing incidence of the x-ray beam can give information about the thickness and roughness of a film. A common wavelength for this is the so called Cu α_1 ($\lambda = 1.54056 \text{ \AA}$) which is also used in the following experiments. The devices used are Bruker D8 XRD, PANalytical X'Pert Pro and PANalytical X'Pert Powder.

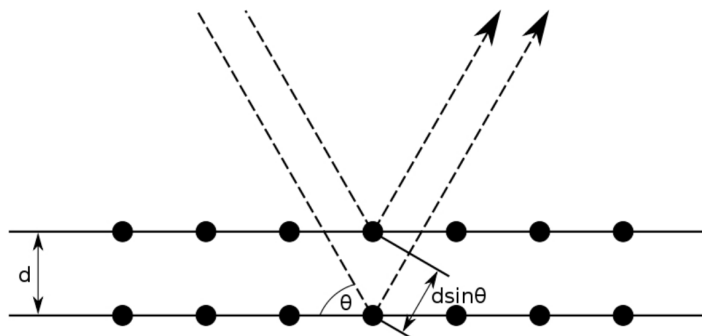


Figure 2.11: Illustration of the Bragg Law

2.4 Thin film deposition techniques

2.4.1 Pulsed laser deposition

Pulsed laser deposition (in the following named PLD) is a very popular technique for growing thin films of all kinds of materials. An external laser source is focused on the so called targets which are made out of the material to be deposited. The actual reaction of the light with matter takes place in a high vacuum chamber with a controlled gas atmosphere. The laser used here is a Coherent COMPexPro KrF excimer laser that operates with a wavelength of $\lambda=248 \text{ nm}$ and a pulse width of 30 ns. When the light struck the target, the beam energy is converted into thermal, chemical and kinetic energy causing the target material to eject matter as depicted in figure 2.13. If the energy in the focus of the laser is high enough a plasma plume is formed that is highly directed away from the target. A substrate on which the film will be deposited is then placed in the

outer glow of the plasma plume where the molecules are relatively slow so that they will not bounce off the substrate or destroy it on impact. As with all deposition techniques, the circumstances of the environment, in which the film is grown, determine the phase that will be formed.

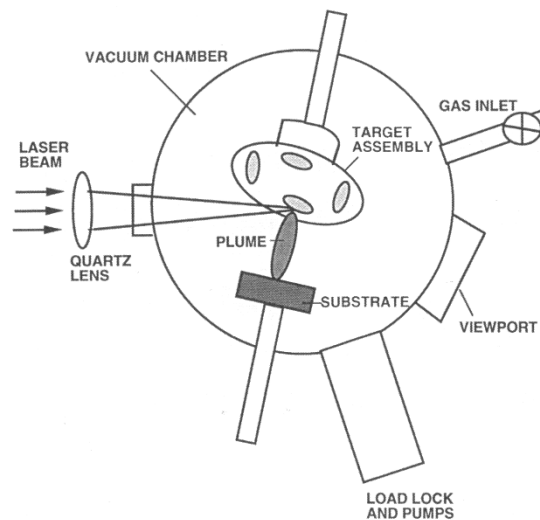


Figure 2.12: Schematic setup of a PLD vacuum chamber. Picture taken from Milton Ohring, Materials Science of Thin Films [9]

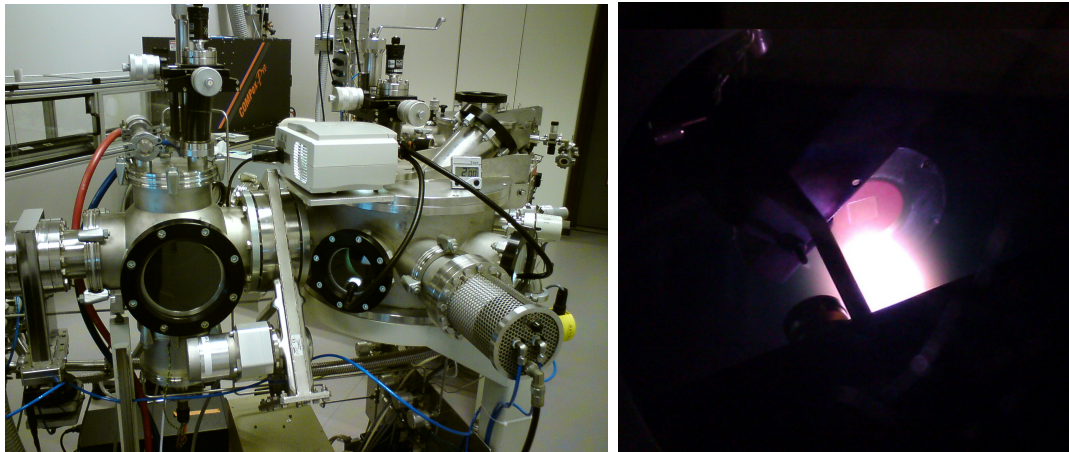


Figure 2.13: Left: the PLD apparatus used for deposition. Right: Deposition in progress, the plasma plume strikes the substrate on a heater.

2.4.2 RF sputtering

Sputtering is another type of deposition process that was used during the course of this project. In this process a gas (e.g. argon) is ionized and accelerated in an electric field. When the heavy ions struck the targets, matter is ejected for deposition and the ions become neutral again. RF sputtering is a special type of the sputtering process in which

2. Theoretical Background

an alternating electric field is used.⁶ This process is especially useful if the target consists of an insulating material that has to be deposited. In figure 2.14 you can see a schematic drawing of a sputtering device.⁷

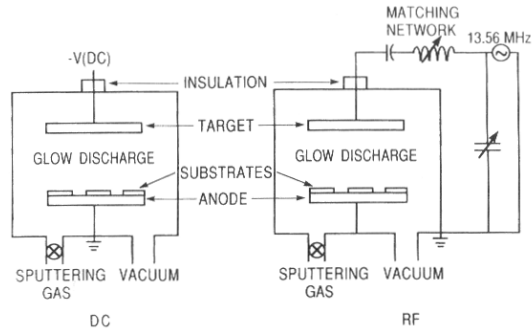


Figure 2.14: Schematic of a sputter process chamber. Left: normal sputtering, right: RF sputtering. Picture taken from [9]

⁶The RF stands for radio frequency.

⁷For more information on the physics of sputtering refer to [9].

Chapter 3

Experimental Work

3.1 Production of a capacitance test circuit

A test circuit was produced for the purpose of understanding the experimental procedures of creating a thin film capacitor. These procedures involved film deposition, lithographic structuring and etching of thin layers of several different materials. Therefore a lithographic mask, that has been used before in a field effect structure¹, was recycled so that the result was a parallel plate capacitor. With this structure the capacitance of several different sized areas can be measured and the dielectric constant of STO can be calculated.

3.1.1 Sample structure

Figure 3.1 shows the layers of the capacitance structure that was produced. YBCO was used as the bottom electrode and Aluminum as the top electrode. STO is the dielectric that has to be measured in this test setup. The purpose of the Silicon oxide is to prevent any short circuits between the top and bottom electrodes. It was chosen because of the relative low dielectric constant (~ 3.9) so that its contribution to the capacitance could be neglected.

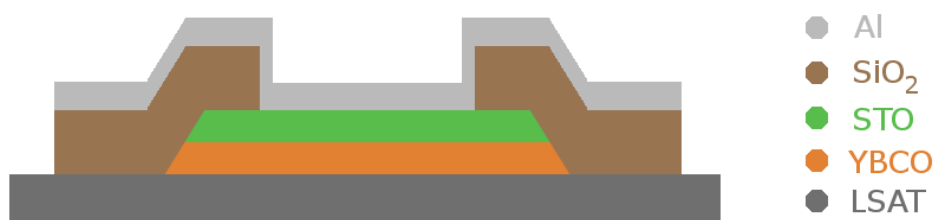


Figure 3.1: Schematic drawing of the thin film layers of the capacitance test circuit

For simplicity the dielectric was placed between the electrodes which were crossing each other in a right angle. The lithography masks that had been used are shown in figure 3.2. A closeup of the structure's main part where the areas are situated that build

¹For more information on an alternative use of the masks refer to [5].

3. Experimental Work

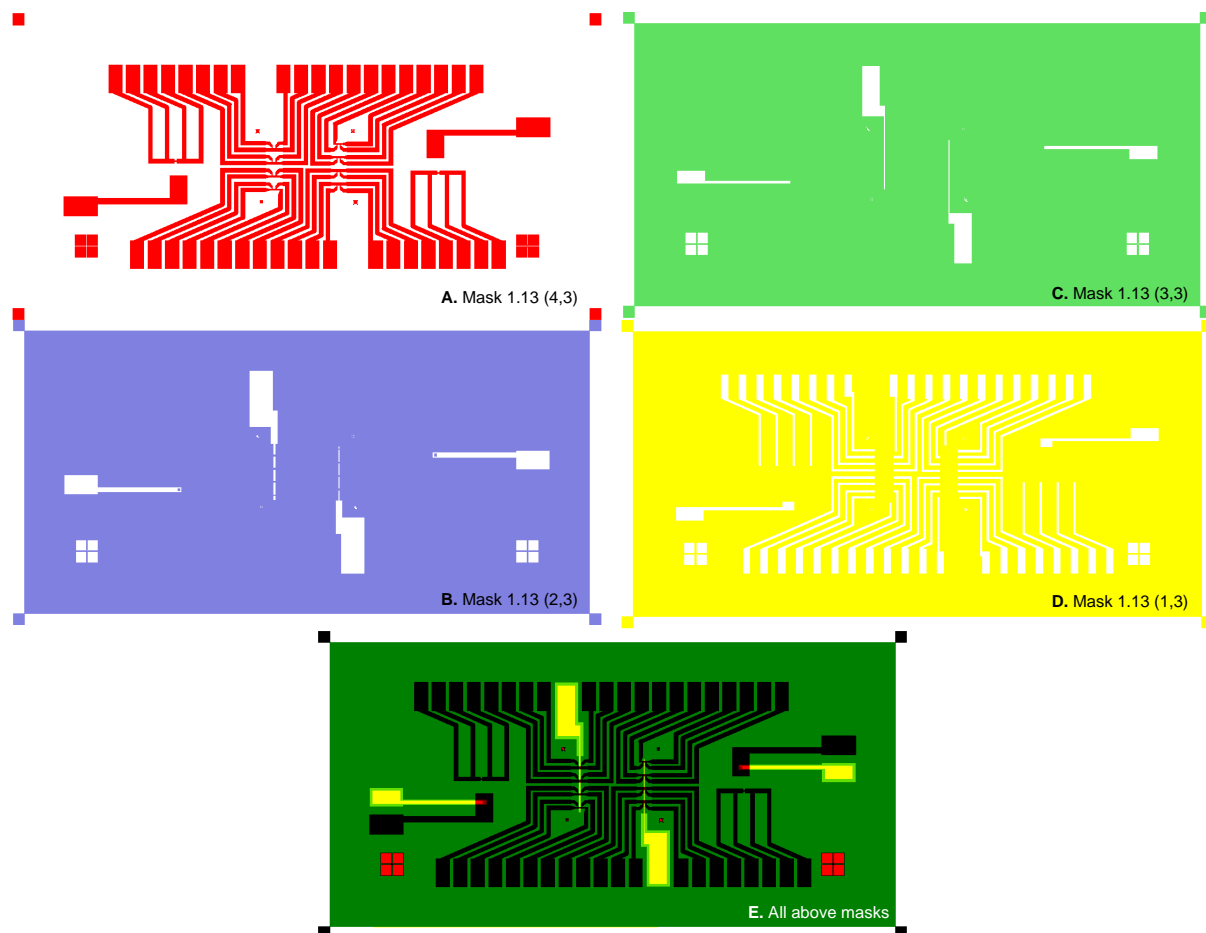


Figure 3.2: Lithography masks used for the capacitance test circuit

up the capacitance is shown in figure 3.3. There is thus one top electrode connection for the thick and one for the thin line areas, opposing four bottom electrode connections for each area itself. These four connections had no further purpose in this experiment, they were just a leftover of the recycled masks.

3.1.2 Thin film circuit preparation

A 1cm^2 by 0.5mm single crystal LSAT was used as a substrate. It was cleaned in an ultrasonic bath for 15 minutes in acetone and 15 minutes in ethanol.

The first step was to deposit a bilayer of YBCO and STO on top of the substrate using pulsed laser deposition (see 2.4.1). It was therefore fixated with silverglue on a special heater that could maintain high temperatures for optimal deposition. The heater was then inserted into a stainless steel high vacuum chamber where the deposition took place. The temperature was read out through the use of a thermocouple right underneath the substrate. With a KrF excimer laser, operating at 248nm and a pulse width of 30 ns , YBCO and directly thereafter STO were deposited according to the settings listed in table A.1. It was expected that under these conditions a 50nm YBCO and a 30nm STO layer were grown. The temperature and pressure diagram of the deposition process is

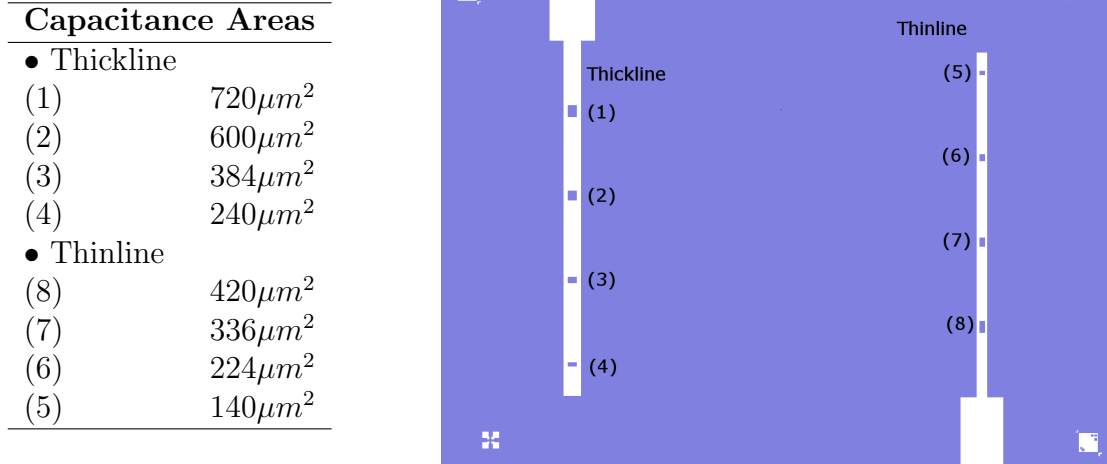


Figure 3.3: Closeup of the capacitor areas on the masks.

shown in figure A.1.

A thick layer ($\sim 1.7 \mu m$) of positive photoresist was spinned at 6000 rpm onto the sample and dried out for 2 min @ $100^\circ C$. Then, the structure of 3.2 (A) was written into the photoresist with the use of a Süß Mask Aligner MA-56. The exposure time of the Hg lamp on the photoresist was set to 8 seconds. The photoresist was developed using Opel 4262 developer.

With this thick layer of photoresist on top, to keep the relevant part of the structure, the bilayer was etched away. Therefore it was assumed that the etch speed of YBCO is similar to the one of STO. When etching with argon according to the settings of table A.3 under an angle of 45° , it had been looked up in the logbook of the etch device, that STO has an etch speed of 2,5 nm/pulse. To be on the safe side 35 pulses were used corresponding to 87.5nm. In figure 3.4 you can see how the film looked like after the etch procedure.

After applying photoresist again and writing the mask (B) into it, SiO_2 was sputtered² in a Perkin Elmer RF sputtering system onto the film according to the settings listed in table A.4. Than the photoresist together with the unwanted part of the SiO_2 was lifted off.

Mask (C) was applied to the structure and the aluminum top electrode was sputtered according to the settings in table A.5. The result can be seen in figure 3.5.

In the last step, mask (D) was applied to etch away the STO layer, so that the YBCO bottom electrode could be accessed by the probes of the measurement device. This was done for about 12 pulses according to the settings in table A.6. This time the etch velocity was adjusted to 3.5 nm/pulse because of the findings of an AFM scan after the first etch procedure.

²See section 2.4.2 for more information on sputtering.

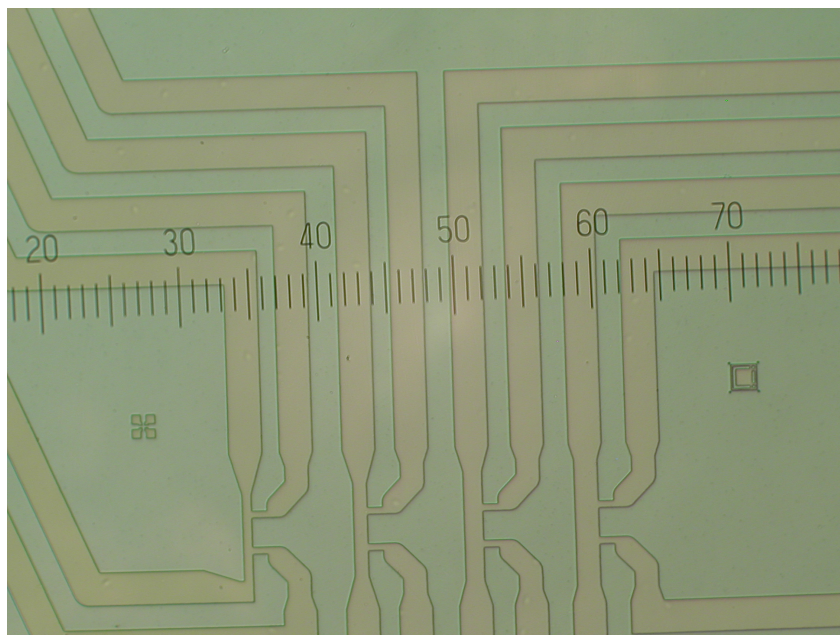


Figure 3.4: The YBCO-STO bilayer film after the etching procedure.

3.2 Solid state synthesis of barium strontium titanate targets for use in laser ablation devices

Because of the properties mentioned earlier, BSTO is very suitable for the production of a high-capacitance structure and should replace STO in the test circuit described above. Since the delivery time was too long, the decision was made to produce a target for the use in a laser ablation device within the group. This required a set of steps that are described in the following.

3.2.1 Reaction and processing

For the reason of safe storage and easy handling, most materials come as compounds in the form of powders. The reagents that were used are listed in table 3.1. Ultra pure reagents were used to achieve high purity targets for the production of high quality thin films.

list of reagents	
BaCO ₃	from an unknown Producer, high purity
SrCO ₃	from Alfa Produkte, 50g, 99.994% purity
TiO ₂	from ESCETE - Single Crystal Technology B.V., Enschede, high purity

Table 3.1: reagents for the production of a BSTO target

Thermal treatment in the form of a calcination process is used to get the desired compound from these powders. In this process volatile fractions of compounds, in this

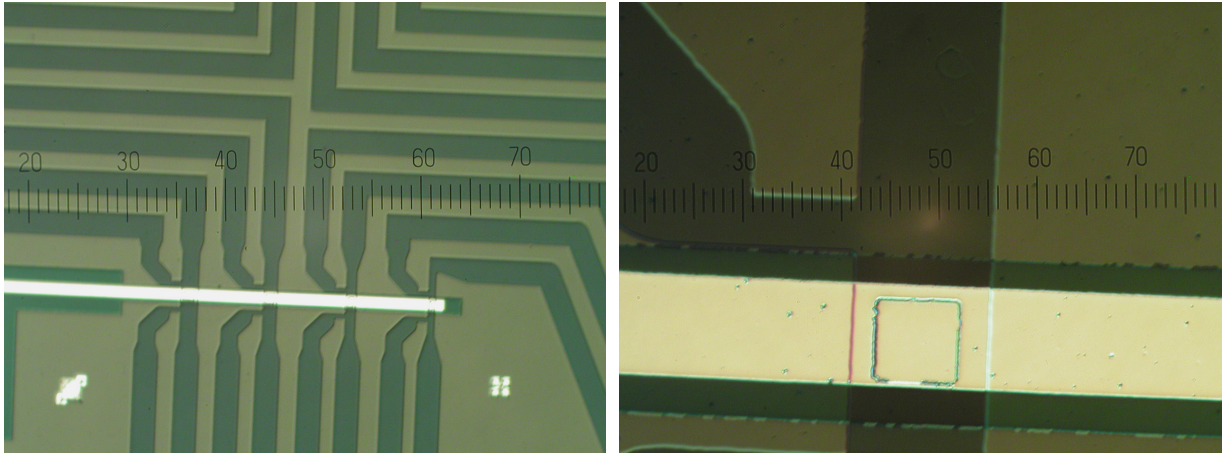


Figure 3.5: The capacitor structure after the sputtering of Al. Note the rectangle in the right picture, which is the area of the parallel plate capacitor just produced.

case the carbon oxide, are removed below the melting point of the products (since the name solid state synthesis).

The desired reaction is the following:



Where there is no need to balance the formula since the reaction takes place in an oxygen rich atmosphere. Two compositions of BSTO were produced, $\text{Ba}_{0.5}\text{Sr}_{0.5}\text{TiO}_3$ (in the following named BSTOx5) and the desired $\text{Ba}_{0.67}\text{Sr}_{0.33}\text{TiO}_3$ (in the following named BSTOx67). After each step of the process a XRD scan of the pellets or powders was made in order to look for impurities.

Weighting In the first step the three powders had to be weighed according to the desired stoichiometry. The goal was to get about 16g of each compound to create one test sample of each and one big target when the tests were successful. The weighting was done on a high precision scale that could measure accurately down to 10^{-4} grams. The calculated and weighed compounds are listed in table 3.2

Mixing and milling In the next step the powders had to be mixed. To get a homogeneous distribution and to decrease the grain size of these powders they were milled in a Fritch Pulverisette 6 planetary ball mill. This was not very effective in the first place because after a short time of milling all the powders stuck at the bottom of the crucible and the balls were rolling over them. By adding 99.97% pure ethanol as a solvent the powders could finally be milled. The powders were mixed in total 90 min: 10 min dry&slow (210,280 rpm) + 10 min wet&slow (120 rpm) + 70 min wet&fast (500 rpm). When going to higher milling speeds the crucibles were becoming slightly warm and the milling was done in 3 min intervals with about 10 min pause inbetween, to prevent any pressure buildup. After the milling procedure the powders were dried at 60°C for about

3. Experimental Work

Powder weights according to the desired stoichiometry of BSTO			
	compound	calculated weight	actual weight
• x=0.5	BaCO ₃	6.2560 g	6.2561 g
	SrCO ₃	4.6802 g	4.6803 g
	TiO ₂	5.0638 g	5.0644 g
• x=0.67	BaCO ₃	8.1113 g	8.1115 g
	SrCO ₃	2.9888 g	2.9901 g
	TiO ₂	4.8997 g	4.9002 g

Table 3.2: Weights of the powders for the solid state synthesis of Ba_xSr_{1-x}TiO₃

2 hours to let the ethanol evaporate completely. In the end there were about 15.5 g powders of each stoichiometry.

Pressing and Sintering For the production of the first BSTO test targets, 4.5 g of the BSTOx5 powder and 3.5 g of the BSTOx67 powder were pressed to pellets with 15 ton and 25 ton respectively in a standard shop press with an 3.14 cm² area piston. Unfortunately these pellets turned out to be very fragile. From literature it was already known that BSTO had to be sintered at temperatures between 1250-1400°C [8] to produce a stable target. Nevertheless, the pellets have been heated for 9 hours at 1150°C, which was 50°C below the maximum temperature that could be achieved in the Vecstar Furnace used. Figure 3.6 shows SEM pictures taken after this synthesis.

These pictures show that the grain size is in the order of μm but the density is quite low, what explains why the pellets fell apart. Apparently something had to be done to get a higher density when pressing the powder into pellets. After crushing the pellets they were milled by hand for about 30 min until they reached a creamy consistency. It was then tried to add a few drops of a polyvinyl alcohol solution³ as a sort glue to the powders. Actually it can't be said how much PVA was used since the pipette had no scale. In this case 11 drops were added on 3.3 g BSTO powder. However the consistency of the powders should be a little bit more creamy than before. The powders were than successful pressed at 20 ton (BSTOx5) and 25 ton (BSTOx67) and dried at 80°C for half an hour before going up to 350°C at a ramp rate of 5°C/min where they were again maintained in an oxygen atmosphere for 30 minutes to let the polyvinyl alcohol evaporate. Than again with a ramp rate of 5°C/min the pellets were heated up to 1200°C to start the second sintering process. The pellets were kept at this temperature for 24 hours. SEM pictures after the second synthesis are shown in figure 3.7. From this pictures it is clear that the density was increased and that the grain size is of the order μm . Unfortunately the BSTOx67 pellet was cracked after the second sinthering. This might be because there was a little bit too much PVA added to the powder and it was pressed at a higher pressure.

Knowing all the difficulties in the process, there were two more targets produced from the rest of the powders. One BSTOx5 target from 8.0 g powders and one BSTOx67

³A solution of 3% PVA 61K in H₂O was used.

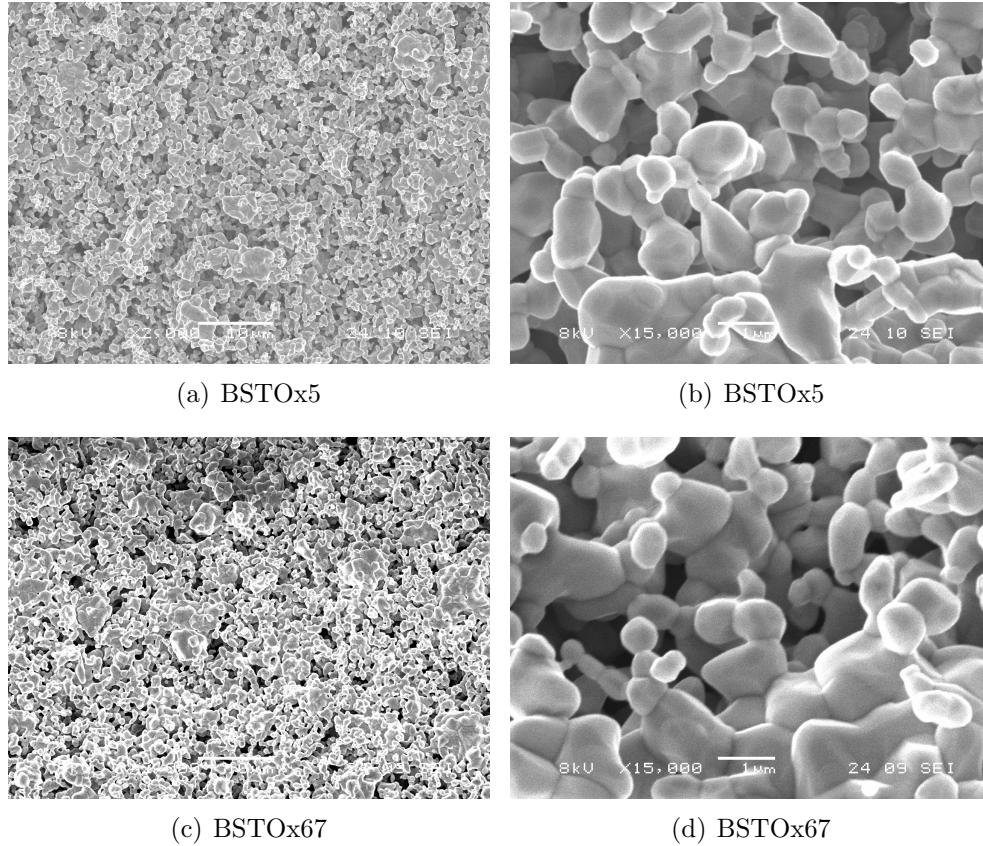


Figure 3.6: SEM images of the BSTO pellets after the first sintering/synthesis procedure

target from 8.2 g powders. Both were first sintered in powder form for about 18 hours at 1150°C. Then again PVA was added and both were pressed at 20 tons. This time 26 drops of PVA were added to the BSTOx5 and 28 drops of PVA to the BSTOx67. As the pellets were pressed the BSTOx5 was all white and the BSTOx67 showed grayish surface at the border.⁴ The pellets were then first dried at 65°C for 40 min, before heating them for one hour at 350°C and then finally sintered 24 hours at 1200°C. As usual the ramp rate was 5°C/min and the preheating removed the PVA.

3.3 Target testing and film growth

Due to lack of time and because of the crack in the first test target of BSTOx67, it was only possible to test the performance of the BSTOx5 test target. The aim was to grow a first film of BSTOx5 on a LSAT substrate.

3.3.1 Determination of energy flux

The first step was to determine the energy flux of the laser pulse that should hit the target to generate the plasma plume required for deposition of BSTO onto a substrate.

⁴Looking at this part with the SEM after the second sintering, it there was no difference in contrast to the normal, white part of the surface.

3. Experimental Work

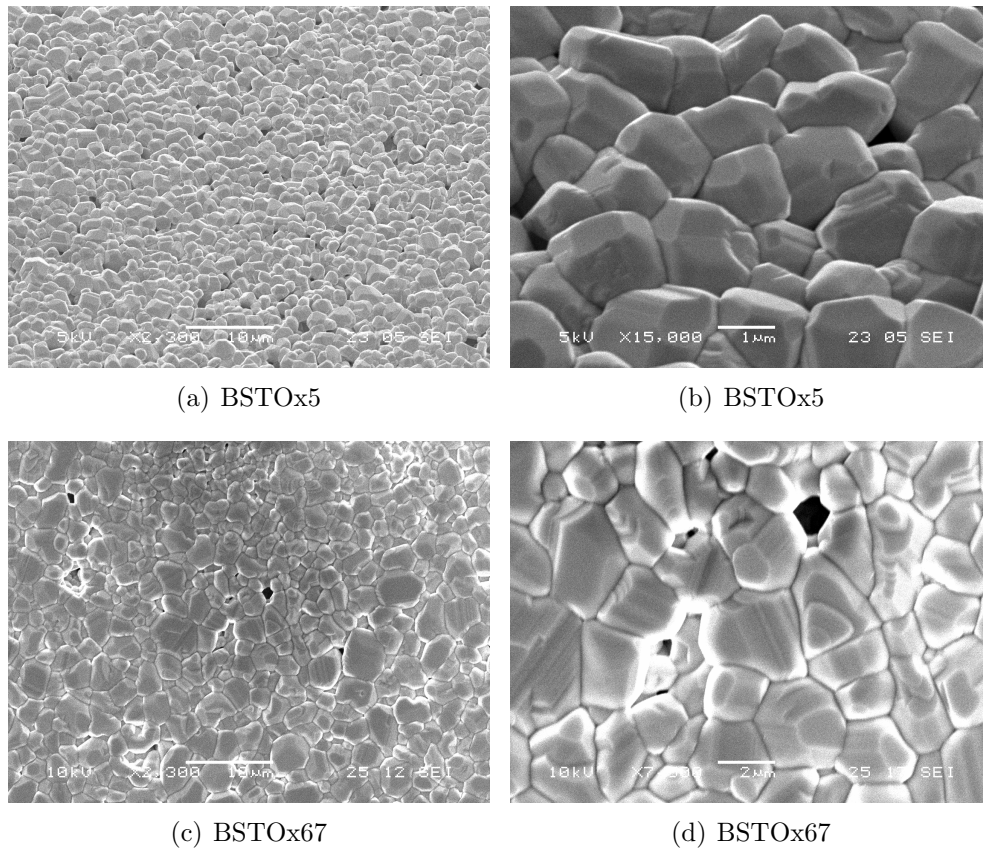


Figure 3.7: SEM images of the BSTO pellets after the second sintering procedure

The target was therefore shot with four different energy fluxes at a fixed pressure of 0.13 mbar and afterwards analyzed with the SEM microscope (see figures 3.8, 3.9 and 3.10). The observations are summarized in table 3.3. The pictures for a energy flux of 4 J/cm^2 were omitted since the surface did not change much with respect to 2 J/cm^2 . From the pictures and observations it is clear that the perfect value lies somewhere between 1 and 2 J/cm^2 . This also matches values found in literature [6].

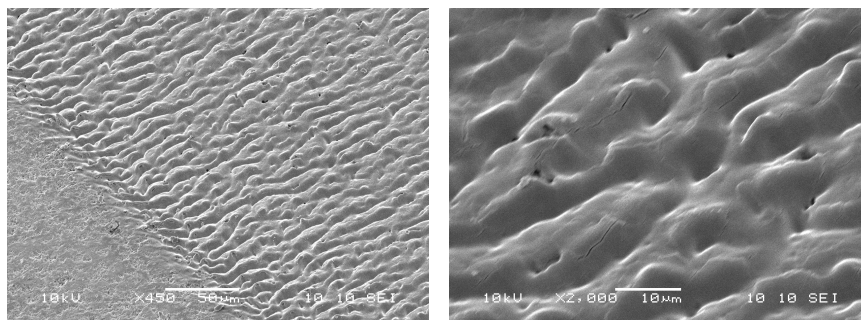


Figure 3.8: Laser ablated BSTOx5 at an energy flux of 0.5J

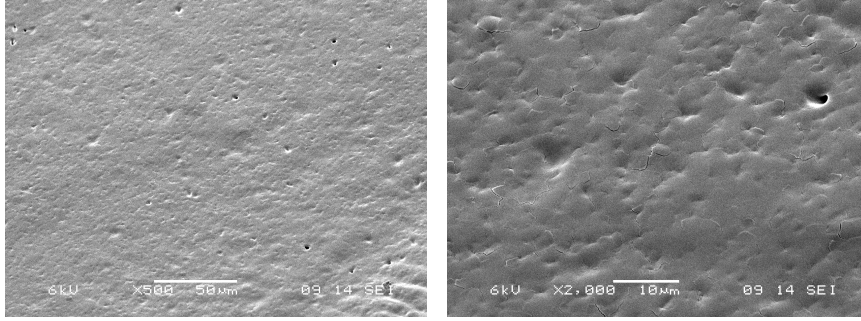


Figure 3.9: Laser ablated BSTOx5 at an energy flux of 1J

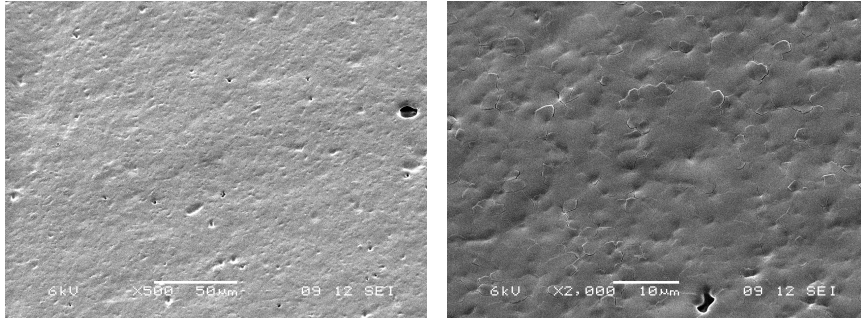


Figure 3.10: Laser ablated BSTOx5 at an energy flux of 2J

3.3.2 Film deposition of BSTOx5

The first film that was grown from the BSTOx5 target was deposited similar to the settings in table A.7. But since the distance to the substrate had to be determined this was adjusted together with the background pressure from 50 mm and 0.10 mbar to 62 mm and 0.13 mbar at half the ablation time. The total ablation time was 180 seconds @ 4 Hz and thus 720 pulses in total. Since the growth conditions were very similar to STO conditions, it was expected that the growth velocities were similar, too. So this should result in a film thickness of about ~ 72 nm. Unfortunately a XRD-reflectivity scan could not be fitted with a curve and so it was not possible to determine the thickness and thus the growth speed.

The second film was grown at a fixed distance and background pressure as listed in table A.7. This time was the substrate positioned right in the yellow corona of the plasma

Flux determination observations				
Energy fluency (J/cm^2):	0.5	1	2	4
Plasma plume visible:	yes	yes	yes	yes
Plasma size (cm):	~ 2.5	~ 4.5	~ 5	~ 6
Plasma colour:	white	yellow core	blue core and yellow corona	purple/blue core

Table 3.3: Fluency observations. Settings: 100 pulses, 0.13 mbar O_2 .

3. Experimental Work

plume from the beginning on. The deposition time was only 88 seconds @ 4 Hz because it was assumed that the reason for the bad XRD-reflectivity scan was that the film had been too thick to get clear oscillations. The films have been analyzed with AFM and XRD techniques and the results are presented in the following chapter.

Chapter 4

Results and discussion

4.1 Capacitance test circuit

4.1.1 Production

During the production of the capacitance test circuit, several analysis techniques were applied to get information about the thin films. After the first step of growing the YBCO-STO bilayer, a tapping mode AFM scan revealed that it had a rather rough surface (in the order of ~ 6 nm) as depicted in figure 4.1.

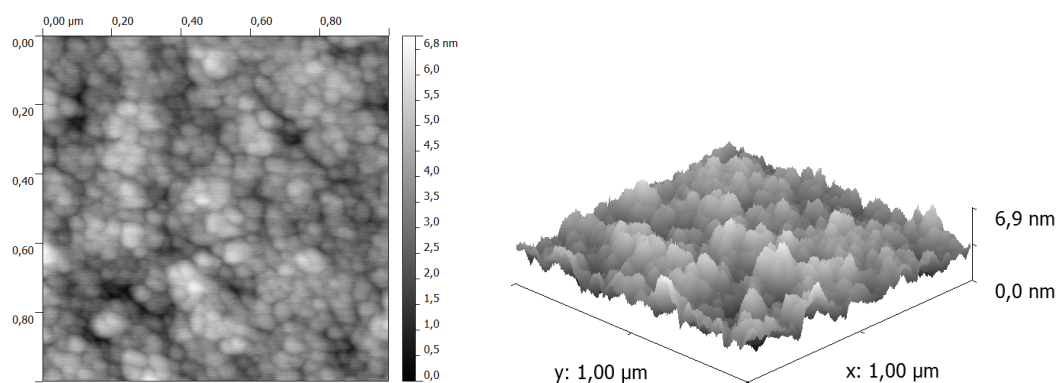


Figure 4.1: An AFM scan of the capacitance test circuit directly after the deposition of the YBCO-STO bilayer.

The next analysis was an XRD scan to determine the thickness of the independent layers and the orientation of its crystals. From the 2θ scan depicted in figure B.1 it can be concluded that YBCO was grown in the [001] direction and STO in the [100] direction. With the help of the computer program Leptos¹ it was not possible to fit a theoretical model to the data recorded by a XRD reflectivity scan. The closest, but unsatisfactory fit was $d_{STO} = 33\text{nm}$. Therefore the thickness of both layers could not be determined by this method. Since this method is normally quite reliable, this was evidence for inhomogeneities in the films.

¹Provided by the manufacturer of the x-ray spectrometer Bruker.

As mentioned in 3.1.2, the etch conditions have been assumed to be equal for YBCO and STO. Because this was done to get a lower limit of the etch time, one could expect to see different slopes on the etched borders of the structure. Therefore an AFM scan was done on the outer contacts on the upper left and on the lower right of the structure. Height profiles of the scans are shown in figures 4.2 and 4.3. The layers under the horizontal parts are from left to right YBCO-LSAT, STO-YBCO-LSAT, LSAT. Unfortunately there can not be drawn any conclusion about the thickness of the single layers. The differences in the slopes are so small that they might be also due to shadow effects of the etch procedure². It might give only an upper bound on the thickness of the STO film of about 55 ± 2 nm.

But actually there is another conclusion that can be drawn from the AFM scans. Note that the deviation in height of the upper part is only of the order of 4 nm (which is also the order of the surface roughness) while the deviation of the lower part is in the order of 25 nm. This means that the YBCO layer was not deposited with a uniform thickness which can be explained with the variation in the target substrate distance during the deposition (see table A.1). There was also a colour gradient observed in the bilayer that can be explained this way (see figure 3.4). This gradient varied from the lower left to the upper right from blue to brown.

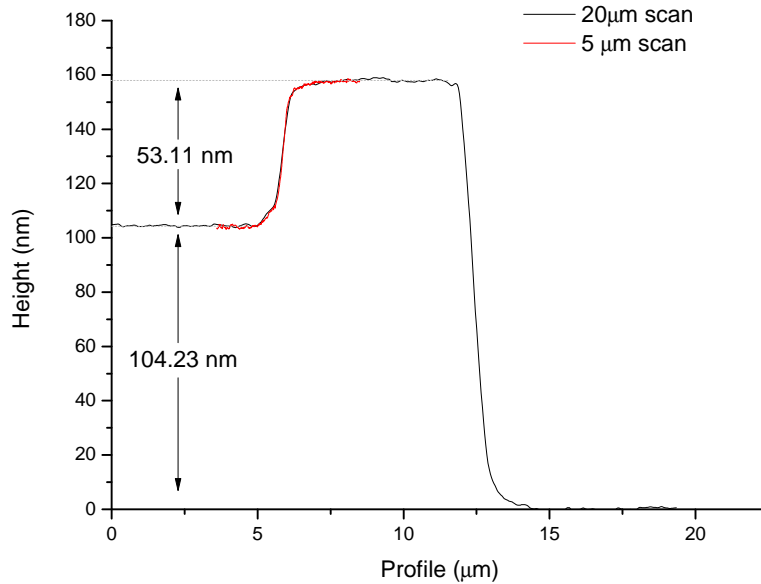


Figure 4.2: An AFM scan of the upper left part of the bilayer structure.

4.1.2 Capacitance measurements

Having produced the thin film capacitor the time had come to measure what had been achieved. As already mentioned, two types of measurements were made. The quasistatic

²Recall that the etching was done under an angle of 45°

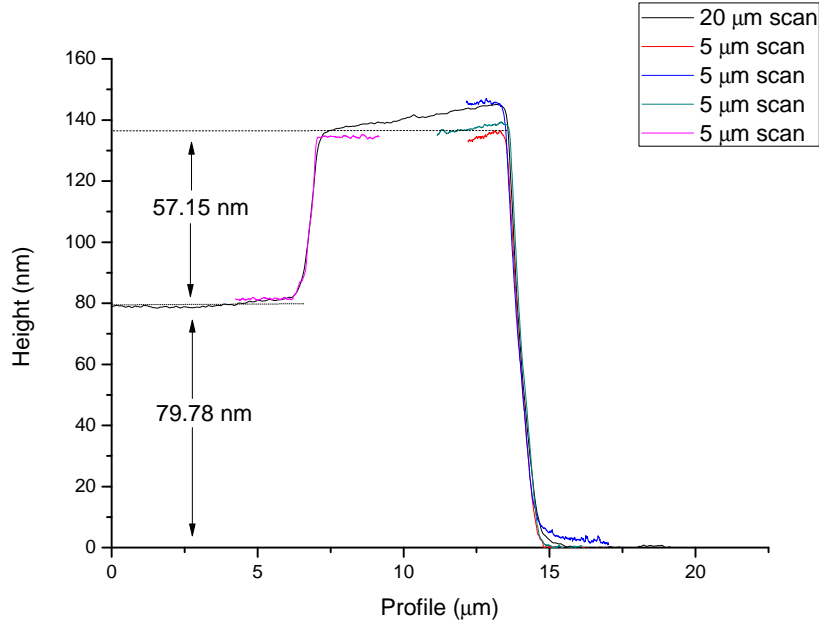


Figure 4.3: An AFM scan of the lower right part of the bilayer structure.

capacitance measurements were carried out in the Semiconductor Components group of Jurriaan Schmitz. Here the Keithley 595 quasistatic CV meter was used by connecting the needles of a Süss Microtec PM300 probestation with our test circuit. The measurement had been carried out according to the standard procedure from the manual. The frequency dependent measurement was carried out in the nanolab labs using the Philips PM 6303 RCL meter connected to an older, unknown type of a Süss probestation.

Both measurements were used to calculate the capacity per area (C/A), the dielectric constant (ϵ_r) and the Capacitance Equivalent Thickness (CET). The CET indicates how thick a layer of SiO_2 would have been to achieve the same capacitance. It is calculated according to

$$CET = \epsilon_0 \epsilon_{\text{SiO}_2} \frac{A}{C} \quad (4.1)$$

where $\epsilon_{\text{SiO}_2} = 3.9$. For calculating ϵ_r a layer thickness of 33 nm was used. Both measurements are plotted in figure 4.5 Due to contact issues with the needles in both probestations, some values have been excluded when calculating the mean values.

The following results have been obtained by averaging the non excluded values. For the quasistatic measurements: $\epsilon_r = 175.16 \pm 1.13 \mu\text{F}/\text{cm}^2$, $C/A = 4.70 \pm 0.03 \mu\text{F}/\text{cm}^2$ and $CET = 0.738 \text{ nm}$. For the measurement at 1kHz: $\epsilon_r = 143.39 \pm 3.11 \mu\text{F}/\text{cm}^2$, $C/A = 3.85 \pm 0.08 \mu\text{F}/\text{cm}^2$ and $CET = 0.905 \text{ nm}$.

The difference in this values might be explained due to the frequency dependence of the STO dielectric. Comparing the obtained values with those found in literature ($\epsilon_{r,STO} = 332$ from [2]) one notes that the literature values are almost twice as much. One reason to explain this might be that the growth conditions used were not optimal to achieve a high polarize able film of STO. Another possibility is that the film was not thick

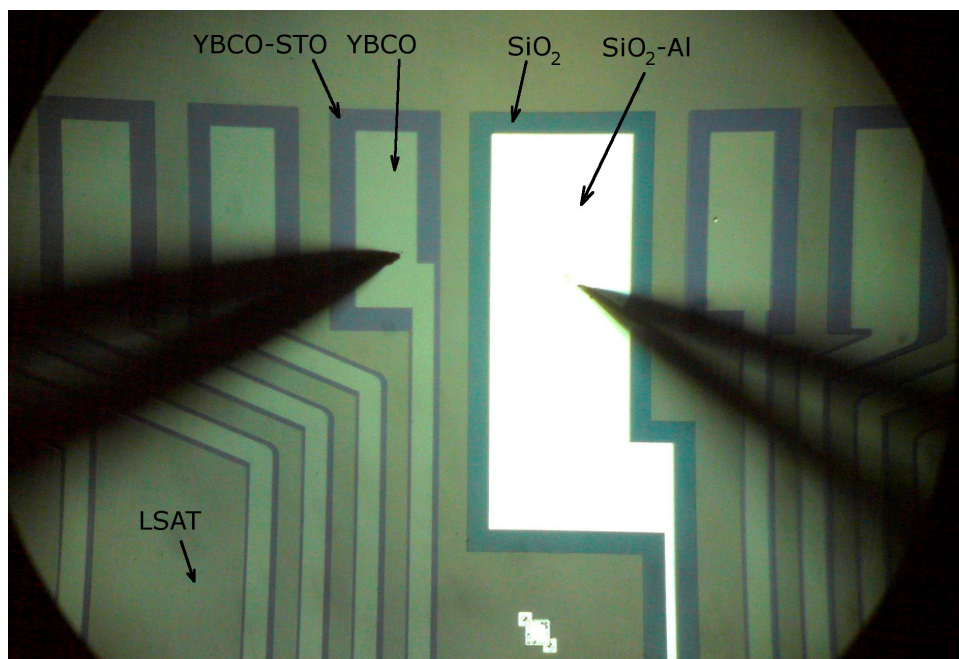


Figure 4.4: A look through the microscope while measuring the capacitance. The two needles make contact with the electrodes of the capacitance test circuit.

enough to reach the full bulk values of the capacitance. A thickness of 33nm correspond to about 84 unit cells of STO which might be too less.

There were some other measurements made with other equipment at a frequency of 100Hz, but results from these measurements were not consistent and are here fore omitted.

4.2 Barium strontium titanate targets for the use in laser ablation growth techniques

4.2.1 Target Preparation

In the course of preparing the targets, XRD scans have been made after each step to check for the purity of the compounds. Since BSTOx5 and BSTOx67 are essentially the same crystals the peaks appear at the same positions of a 2θ scan. Various scans are plotted in figure B.2, containing one scan of the compound in powder state. The hill at the beginning of this scan is due to reflections from the glass of the container used to scan the powders. All these scans show that only the desired compound is formed without any crystalline impurities.

A mean grain size of $2\ \mu\text{m}$ in the case of the BSTOx5 and $3\ \mu\text{m}$ in the case of the BSTOx67 can be determined from figures 3.7 (b) and (d). The densities of the BSTOx5 and BSTOx67 test targets was determined to be 4.68 and 4.65 g/cm^2 respectively. Comparing this with the theoretical single crystal target density with 84.1% and 81.5% quite high density targets were achieved with this method. This density might be increased even further with adding another sintering process and tuning of the pressing pressure. However, since those targets are normally made at higher temperatures could be found.

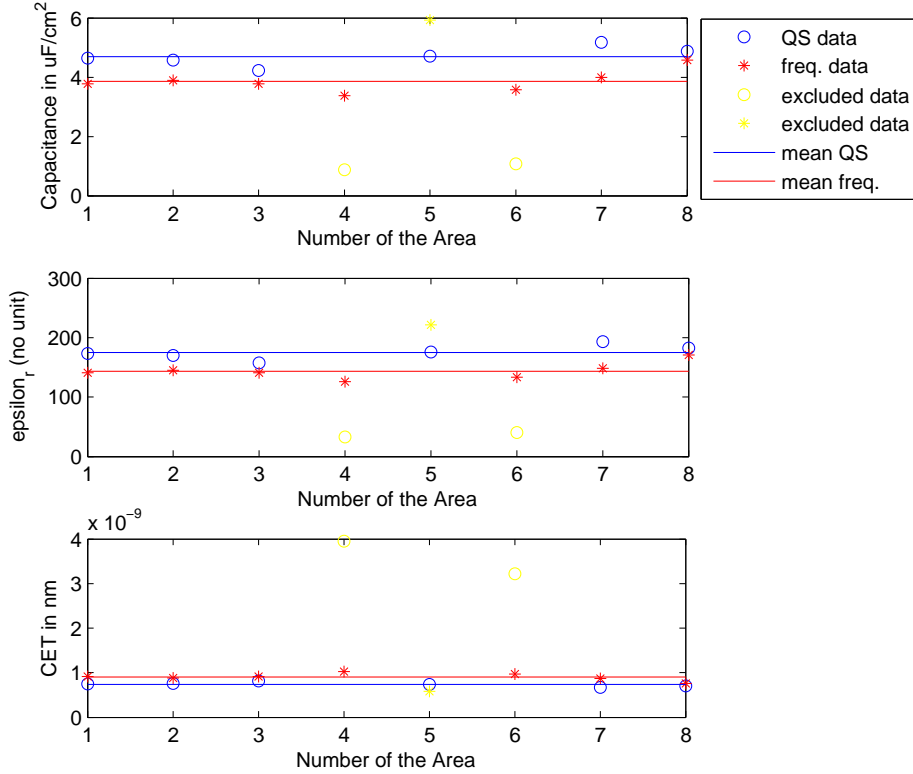


Figure 4.5: Calculated values from the Quasistatic measurements (QS data) and frequency measurements (freq. data). The numbers on the x-axis correspond to the areas in figure 3.3.

where the sintering might be more effective, only a slight increase in the density could be expected.³

However, L. Nedelcu, et al., reports an increase in the dielectric constant due to the sintering of BSTO at temperatures ranging from 1250 to 1400°C. At higher temperatures the adhesive forces of the crystals during the sintesis procedure increase and thereby the density of the target. This indicates that higher densities are necessary to produce higher capacitance films of BSTO.

4.2.2 Grown Films

In figure 4.6 you can see an AFM scan of the surface of the first film grown from the BSTOx5 test target. The roughness of the film is about 3 nm meaning that it has a rather smooth surface.

A 2θ XRD scan revealed that both films from the BSTOx5 test target were grown in the [100] direction on the LSAT [200] substrate (see figures B.3 and B.4). The peaks of the first film were rather broad and exhibit Kiessig fringes. These fringes occur due to repetitive reflections inside the film. These fringes were also present in the scan of the

³Note, no literature on synthesis of BSTO below 1250°C could be found.

4. Results and discussion

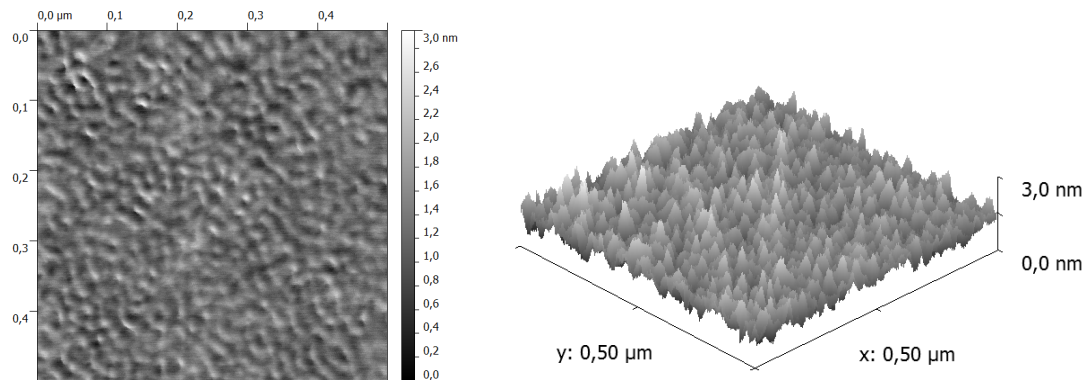


Figure 4.6: AFM scan of the first film grown from the BSTOx5 test target.

second film but in this case the peak was sharper and there were less fringes (see figure B.6). This difference might be caused by the variation of the distance between target and substrate in the first growth procedure. This means that the second film was grown more homogeneous than the first one.

As mentioned earlier, a reflectivity scan of the first film could not be fitted on a theoretical model and so a second film was grown. This time a fit was possible although the values were not as expected (see figure B.5). It turned out that the film was 13.11 nm thick and had a density of $\rho_{BSTOx5} = 6.70 \text{ g/cm}^2$, from which a growth speed of 0.037 nm/pulse follows. Furthermore the density that follows from this fit is quite similar to the density of the substrate ($\rho_{LSAT} = 6.74 \text{ g/cm}^2$). This is a rather unexpected outcome since the misfit of BSTOx5 grown on LSAT in the [100] direction is quite small $f = -0.0238$.

Chapter 5

Conclusions and Final remarks

5.1 Conclusions

A high capacitance thin film structure was produced within the research group Interfaces and Correlated Electron systems of the University of Twente. Here fore strontium titanate was used as a dielectric material. The capacity per area (C/A) of this structure was measured in two ways and found to be for the quasistatic measurement $C/A = 4.70 \pm 0.03 \mu\text{F}/\text{cm}^2$ and for the measurement at a frequency of 1kHz $C/A = 3.85 \pm 0.08 \mu\text{F}/\text{cm}^2$.

In order to increase this values strontium doped barium titanate was synthesized in two different stoichiometries ($\text{Ba}_{0.5}\text{Sr}_{0.5}\text{TiO}_3$ and $\text{Ba}_{0.67}\text{Sr}_{0.33}\text{TiO}_3$) by the solid state synthesis method below 1200°C . To be able to produce a stable target for the use in a laser ablation device, polyvinyl alcohol was added to the powders before pressing pellets at 20 and 25 ton respectively. After the second sinthering the $\text{Ba}_{0.67}\text{Sr}_{0.33}\text{TiO}_3$ pellet was cracked and so only growth conditions of the $\text{Ba}_{0.5}\text{Sr}_{0.5}\text{TiO}_3$ target were determined. It was found that by the use of a KrF excimer laser with a wavelength of 248nm and a pulse width of 30ns, an energy flux of $1.5 \text{ J}/\text{cm}^2$ was suitable in an 0.13 mbar O_2 atmosphere. For a deposition on a 700°C heated substrate this values lead to a growth speed of 0.037 nm/pulse.

5.2 Future outlook

Unfortunately a measurement of the dielectric properties of the BSTO targets could not be done. It is recommended that for further research on this, a new structure should be used that can be produced with less steps than the method described above. Also should be pointed out that there should be no variation of the target-substrate distance during deposition, since this leads to inhomogenously grown films.

Furthermore should be looked at the effects on the thickness of the STO of BSTO layers to make a distinction between the bulk and surface behaviour of the dielectrics.

Another very interesting use of the produced BSTO targets is the combination with LaAlO_3 . Research within the ICE group showed that this material forms a conducting gap when there is STO grown on it. This depends strongly on the configuration of the lattice at the boundary surface. It might therefore be interesting to investigate what happens when STO is replaced by similar material.

Appendix A

Device settings

A.1 Production of the capacitance test circuit

Laser ablation parameters		
Device	PLD Etch Combi	
Date	06-05-2011	
Substrate	LSAT	
Target	YBCO	STO
Background pressure (mbar)	$2 \cdot 10^{-6}$	$2 \cdot 10^{-6}$
Mask type	7 holes	7 holes
Mask position	655.76	655.76
Mirror position	140	140
Lens position	34.04	34.05
Spot size (mm^2)	6	6
Pre ablation (min, Hz)	2, 10	2, 10
Distance target/substrate (mm)	59 \rightarrow 63	59
Heater temperature ($^{\circ}C$)	780	740
O ₂ flow (ml/min)	20	10
Process pressure (mbar)	0.2	0.1
Laser energy (kV)	22.9	22.9
Energy behind lens (mJ)	98.6 ± 0.5	98.6 ± 0.5
Energy density (J/cm^2)	1.5	1.5
Deposition frequency (Hz)	4	4
Ablation time (min,s)	2,5	1,15
Estimated thickness (nm)	50	30
Cooldown or annealing gas	O ₂	
Cooldown or annealing pressure (mbar)	1000	
Cooldown or anneal time,temperature	15,600 and 30,430	
Rampdown ($^{\circ}C/min$)	10	
Laser window check (%)	0.91	

Table A.1: PLD growth conditions of YBCO-STO bilayer

A. Device settings

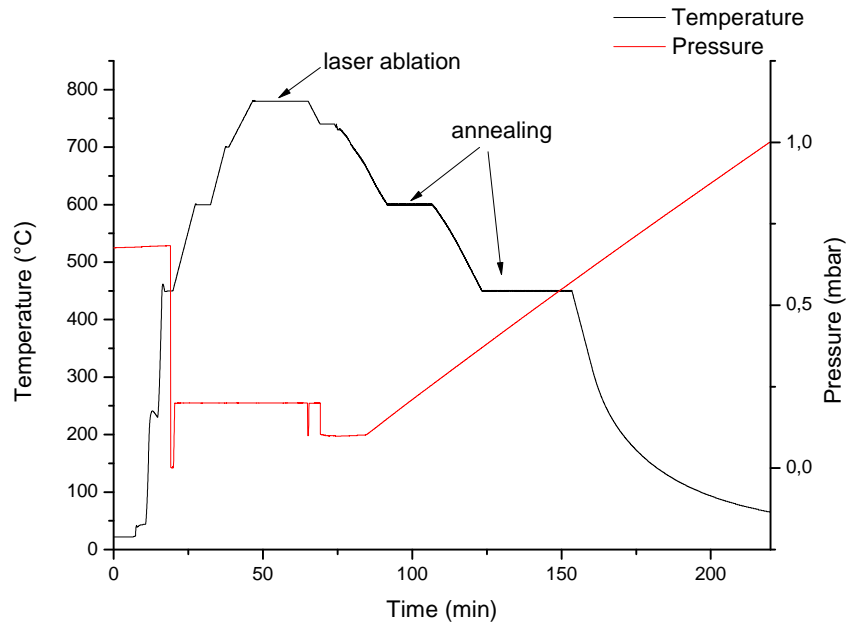


Figure A.1: Temperature and pressure during the YBCO-STO laser ablation procedure.

AFM settings	
Date	06-05-2011
Materials	LSAT-YBCO-STO
Process	AFM
Scan size (μm)	1.00
Offset	0
Scan angle	0
Scan rate (Hz)	1
Integral gain	1.000
Proportional gain	2.000
Drive amplitude (mV)	355.8
Drive frequency (Hz)	292.8399
Lock in phase	121.4 °
Z-range (μm)	1

Table A.2: Settings of the AFM for analyzing the YBCO-STO Bi-layer

Argon etch conditions for 30 nm STO - 50 nm YBCO etching	
Date	09-05-2011
Materials	LSAT-YBCO-STO
Process	etch
P_{back} (mbar)	$5.5 \cdot 10^7$
X position	15.5
Y position	15
Z position	16.5
ϕ	45°
Ar flow	10
On/Off	8:2
Petch (mbar)	$6.4 \cdot 10^4$
V_{beam} (V)	500
V_{acc} (V)	100
V_{dis} (V)	40
I_{dis} (A)	0.36
I_{fil} (A)	4.41
I_{beam} (mA)	10
# Pulses	35
Etch time	8 min + 3 min and 4 s
Assumed etchvelocity for YBCO and STO	2.5 nm/pulse

Table A.3: Argon etch conditions for STO-YBCO etching (step 6)

A. Device settings

Sputtering conditions of SiO₂				
Date	10-05-2011			
Process	substrate cleaning - target cleaning - cooling - sputtering deposition			
P _{background} (Torr)	7.4 · 10 ⁻⁷			
• Substrate cleaning				
Table position	etch	PRF (W)	100	
Table spacing	1.7"	V _{target} (V)	210	
Mode	Sputter Etch	Time (min)	1	
Etch Station	Upper	Target	etch	
Ar (ml/min)	24.5	P _{etch} (mTorr)	20	
• Target cleaning				
Table position	etch	PRF (W)	300	
Table spacing	1.7"	V _{target} (V)	270	
Mode	Sputter Deposit	Time (min)	4	
Etch Station	Lower	Target	SiO ₂	
Ar (ml/min)	22.5	P _{sputter} (mTorr)	21	
O ₂ (ml/min)	12			
• Cooling				
Time (min)	5			
• Sputtering deposition				
Table position	SiO ₂	O ₂ (ml/min)	12	
Table spacing	1.7"	P _{sputter} (mTorr)	21	
Target	SiO ₂	Ar (ml/min)	22.5	
Thickness SiO ₂ (nm)	170			
• Scheme				
Type	Sputter deposit	Sputter deposit	Bias sputter	Sputter deposit
Sputtering time (min)	12.7	12.7	3.2	12.7
PRF (W)	300	350	350	350
Target bias (V)	330	295	350	310
Substrate bias (V)	0	0	50	0
Etch station	lower	upper	upper	lower
Cooling interval (min)	5	5	5	

Table A.4: Sputter settings for SiO₂-sputtering procedure

Sputtering conditions of Al			
Date	11-05-2011		
Process	substrate cleaning - presputtering - sputtering deposition		
• RF substrate cleaning			
Q_{RF} (W)	60	Ar (ml/min)	55.5
V (V)	300	time (min)	2
P_{conv} (mbar)	$1.3 \cdot 10^2$		
• Al presputter at large shutter			
Q_{DC} (W)	75	Ar (ml/min)	38.3
V_{DC} (V)	333	time (min)	5
P_{conv} (mbar)	$0.73 \cdot 10^2$	I_{DC} (A)	0.23
• Al presputter at small shutter			
Q_{DC} (W)	75	I_{DC} (A)	0.22
V_{DC} (V)	339	time (min)	5
• Al deposition			
Q_{DC} (W)	75	I_{DC} (A)	0.21
V_{DC} (V)	352	time (min)	7
rate (nm/min)	28	d (nm)	196
Ion gauge before	$8 \cdot 10^8$		

Table A.5: Conditions for Al sputtering

A. Device settings

Argon etch conditions for 30 nm STO	
Date	12-05-2011
Materials	STO
Process	etch
P_{back} (mbar)	$7 \cdot 10^7$
X position	17.5
Y position	15
Z position	16.5
ϕ	45°
Ar ow	10
On/Off	8:2
P_{etch} (mbar)	$6.5 \cdot 10^4$
V_{beam} (V)	500
V_{acc} (V)	-100
V_{dis} (V)	40
I_{dis} (A)	0.33
I_{fil} (A)	4.33
I_{beam} (mA)	10
# Pulses	12
Etch time	9 min
Assumed etchvelocity for STO	3.2 nm/pulse

Table A.6: Argon etch conditions for STO to YBCO bottom gate etching (step 13)

A.2 Film growth of barium strontium titanate

Laser ablation parameters	
Device	PLD Etch Combi
Date	22-06-2011
Substrate	LSAT
Target	BSTO T1 (x=0.5)
Background pressure (mbar)	$5 \cdot 10^{-7}$
Mask type	7 holes
Mask position	1309.6
Mirror position	140
Lens position	11.69
Spot size (mm^2)	3.5
Pre ablation (min, Hz)	2, 10
Distance target/substrate (mm)	60
Heater temperature ($^{\circ}C$)	700
O ₂ flow (ml/min)	15
Process pressure (mbar)	0.13
Laser voltage (kV)	18.3
Laser energy (mJ)	236
Energy behind lens (mJ)	60 ± 1
Energy density (J/cm^2)	1.5
Deposition frequency (Hz)	4
Ablation time (s)	88
Cooldown or annealing gas	O ₂
Cooldown or annealing pressure (mbar)	1000
Cooldown or anneal time,temperature	15,600 and 30,430
Rampdown ($^{\circ}C/min$)	10

Table A.7: PLD growth conditions of BSTOx5 film layer

A. Device settings

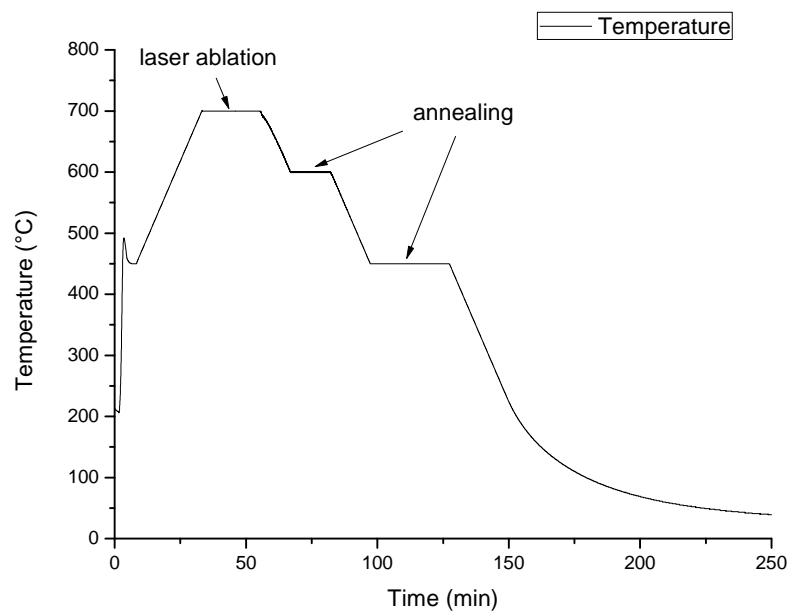


Figure A.2: Temperature and pressure during the BSTOx5 laser ablation procedure.

Appendix B

X-ray diffraction scans

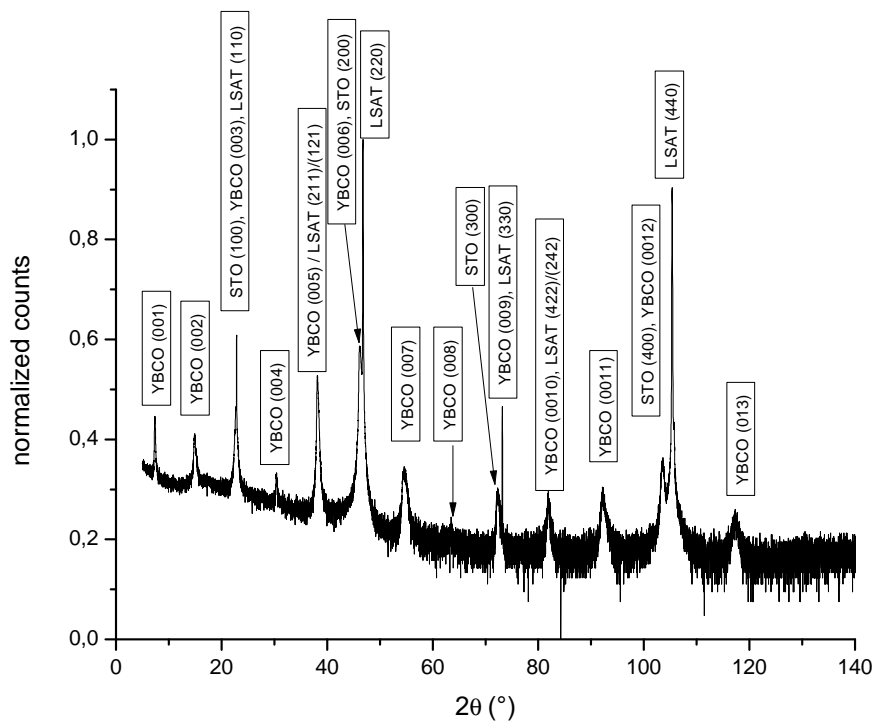


Figure B.1: A 2θ scan of the capacitance test circuit directly after the deposition of the YBCO-STO bilayer.

B. X-ray diffraction scans

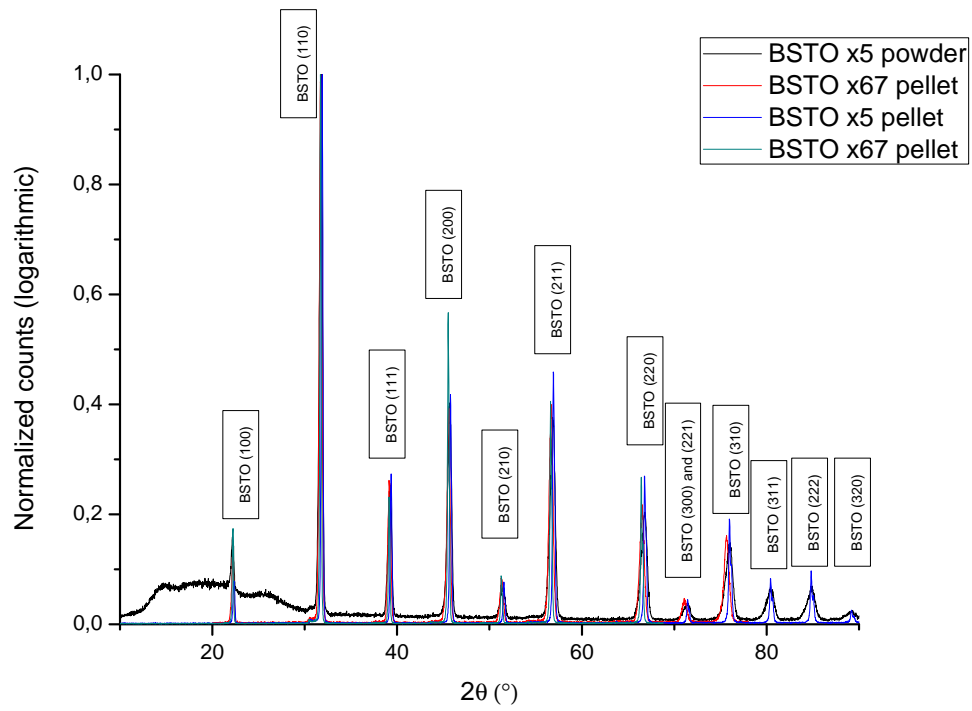


Figure B.2: Various XRD scans were made through out the preparation of the BSTO targets to assure high purity.

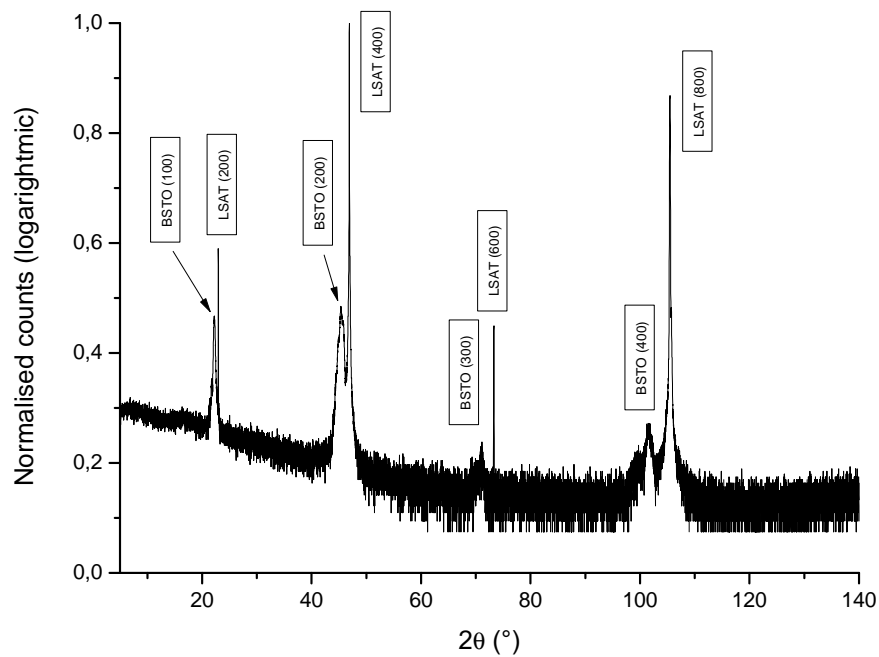


Figure B.3: A 2θ XRD scan of the first film made from the BSTOx5 test target.

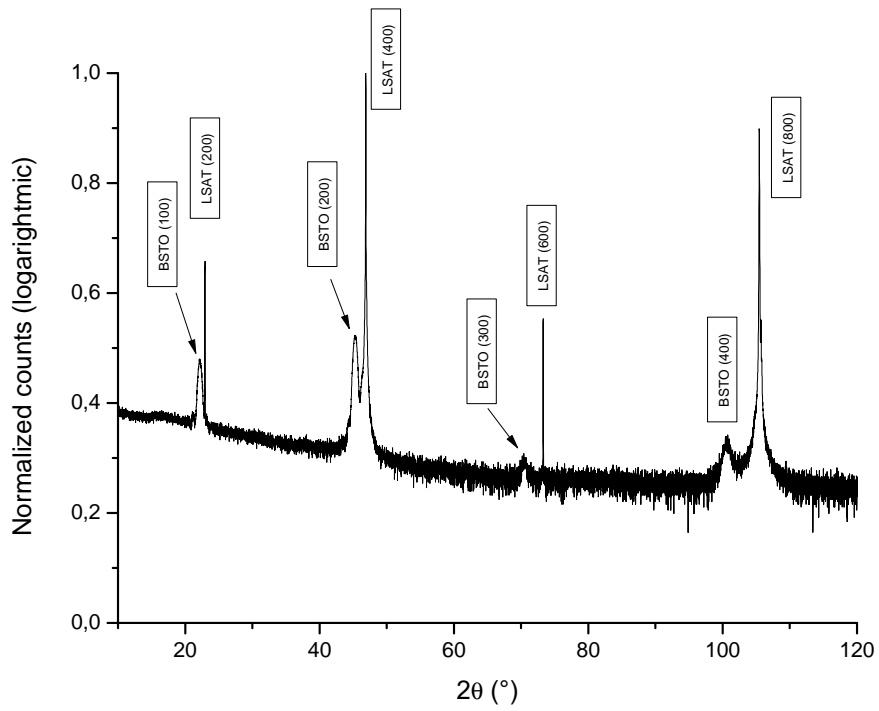


Figure B.4: A 2θ XRD scan of the second film made from the BSTOx5 test target.

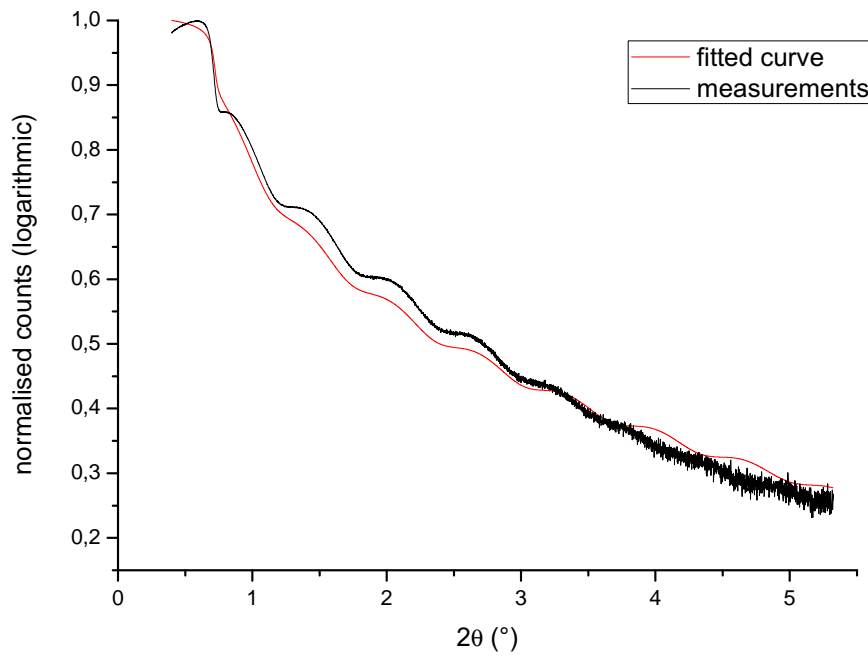
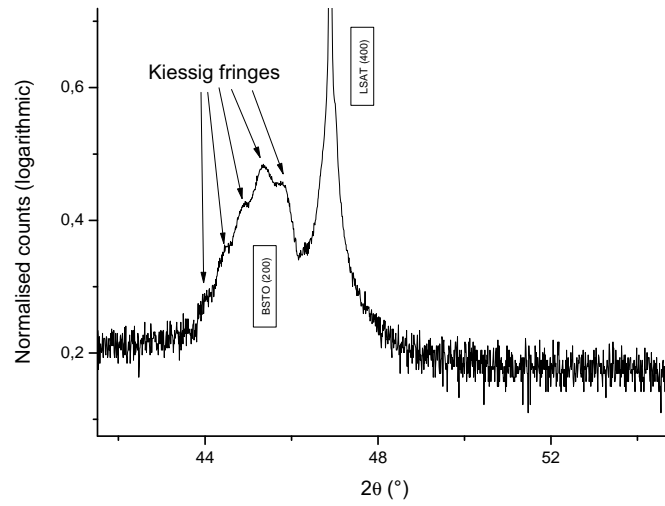
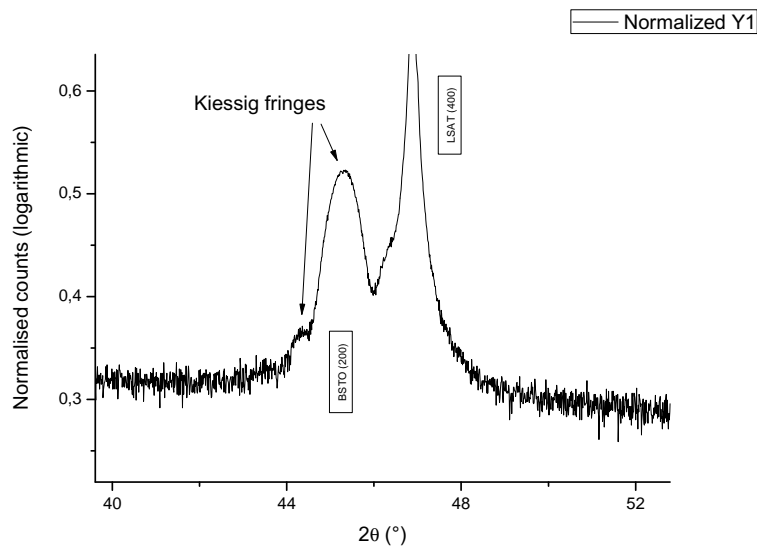


Figure B.5: A XRD reflectivity scan of the second film grown from the BSTOx5 target.

B. X-ray diffraction scans



(a) first film



(b) second film

Figure B.6: A zoom on the [200] peak. The wobbles are called Kiessig fringes.

Bibliography

- [1] Robert L. Boylestad, *Introductory Circuit Analysis*, Prentice Hall, 2002
- [2] *CRC Handbook of Chemistry and Physics*, 91th Edition, Internet Version 2010-2011, <http://www.hbcnetbase.com/>
- [3] D. Fuchs, et al., High dielectric constant and tunability of epitaxial SrTiO₃ thin film capacitors, *Journal of Applied Physics*, 1999, Vol. 85, Nr. 10, 7362-7369
- [4] Kenji Uchino, *Ferroelectric Devices*, Second Edition, CRC Press, 2010
- [5] Wolter Siemons, *Toward electric field effect devices in correlated electron systems*, MSc. thesis, University of Twente, 2004
- [6] Radhapiyari Laishram, et al., Improvement in Electrical Properties of Laser Ablated Barium Strontium Titanate Thin Films by Controlled Oxygen Atmosphere, *Japanese Journal of Applied Physics*, 2009, Vol 48, 061402
- [7] G. E. Moore, *Electronics*, Vol. 38, Nr. 8, 1965
- [8] L. Nedelcu, et al., Synthesis and dielectric characterisation of Ba_{0.6}Sr_{0.4}TiO₃ ferroelectric ceramics, *Thin Solid Films*, 2011, doi:10.1016/j.tsf.2010.12.191
- [9] Milton Ohring, *Materials Science of Thin Films*, Second Edition, Academic Press, 2002
- [10] Keithley Model 595 Quasistatic CV meter, *Instruction Manual*, Keithley Instruments, Inc., 1986
- [11] *Automatic RCL Meter PM 6303A Users Manual*, Fluke, 1995
- [12] Charles Kittel, *Introduction to Solid State Physics*, Eighth Edition, John Wiley & Sons, 2005
- [13] Hu Guoxin, et al, Microstructure and dielectric properties of Ba_{0.6}Sr_{0.4}TiO₃-MgAl₂O₄ composite ceramics, *Ceramics International*, Vol 37-4, 1321-1326, 2011
- [14] Tomokai Yamada, Structural and dielectric properties of epitaxial (Ba,Sr)TiO₃ films on c-Al₂O₃ with ultra-thin TiN sacrificial template, *Journal of the Ceramic Society of Japan*, Vol 119, 261-265, 2011